1 **A Sequential Triple-Drug Strategy for Selective Targeting of p53-Mutant Cancers.**

2

3 Mohammed M. Alruwaili[1,2], Yanqi Guo[1], Justin Zonneville[1], Thomas Melendy[3], Robert M.
4 Straubinger[4,5], Barbara A. Foster[5], Priyanka Rajan[1], Henry Withers[6], Sarah Chatley[7], Renuka
5 Iyer[7], Christos Fountzilas[7*], and Andrei V. Bakin[1*]

6 Author affiliation: [1]Department of Cancer Genetics and Genomics, Roswell Park Comprehensive
7 Cancer Center, Buffalo, New York 14263; [2]Department of Medical Laboratory Technology,
8 College of Applied Medical Science, Northern Border University, Arar City, Saudi Arabia;
9 [3]Department of Microbiology and Immunology, University at Buffalo, 14214, [4]Department of
10 Pharmaceutical Sciences, University at Buffalo, 14214; [5]Department of Pharmacology and
11 Therapeutics, [6]Department of Biostatistics and Bioinformatics, [7]Department of Medicine,
12 Roswell Park Comprehensive Cancer Center, Buffalo, New York 14263.

13 [*]**Corresponding authors:** Andrei V. Bakin, Department of Cancer Genetics and Genomics, Tel.
14 (716) 845-1033; e-mail: Andrei.Bakin@Roswellpark.org; and Christos Fountzilas, Department
15 of Medicine, Tel. (716)845-8974, e-mail: Christos.Fountzilas@Roswellpark.org, Roswell Park
16 Comprehensive Cancer Center, Buffalo, New York 14263

17 **The Lead Contact**: Andrei V. Bakin, Department of Cancer Genetics and Genomics, Tel. (716)
18 845-1033; e-mail: Andrei.Bakin@Roswellpark.org

19

20 **Conflict of interest**: The authors declare no conflict of interest.
21 **Data availability**: The data, analytic methods, and study materials will be made available to
22 other researchers through supplemental material or upon request.

23

SUMMARY

The tumor suppressor *TP53* gene (p53) is mutated in most human malignancies but existing treatment options are largely ineffective, lack selectivity, and cause toxic side effects. To address these clinical problems, we have developed a two-drug treatment that induces lethal DNA damage and G2-arrest in p53 mutant cancer cells. Here, we present a triple-drug therapeutic strategy that combines our two-drug regimen with a G2-checkpoint kinase inhibitor. The two-drug treatment with TAS102 plus PARP inhibitor (PARPi) acts as an *inducer-amplifier* pair to induce DNA double-strand breaks (DSBs) and a prolonged G2-arrest specifically in p53 mutant cells. Subsequent inhibition of the G2-checkpoint kinases, such as WEE1 or ATR, releases these G2-arrested cells into mitosis, leading to cell death. The delayed administration of a G2-kinase inhibitor provides p53 wild-type cells with time to repair DNA, thereby minimizing toxicity to normal tissues. This sequential triple-drug strategy exhibited robust efficacy in preclinical models of colorectal and pancreatic cancers. Together, our findings illustrate a promising *inducer-amplifier-terminator* triple-drug strategy for targeting p53 mutant malignancies.

KEYWORDS: pancreatic cancer, colorectal cancer, poly (ADP-ribose) polymerase, DNA damage, 5-fluorodeoxyuridine, PARP inhibitor, TAS102, trifluorothymidine

ABBREVIATIONS: BER, base excision repair; CRC, colorectal adenocarcinoma; DSB, double-strand break; EdUrd, 5-ethynyl-2'-deoxyrudine; TFT, trifluorothymidine; HR, homological recombination; MMR, mismatch repair; mPFS, median progression-free survival; OS, overall survival; PDAC, pancreatic ductal adenocarcinoma; SSB, single-strand break.

46 **INTRODUCTION**

47 Colorectal (CRC) and pancreatic ductal adenocarcinoma (PDAC) cancers are among the
48 leading causes of cancer-related mortality worldwide, posing significant global health
49 challenges[1]. Despite improvements in early detection [2], CRC remains a considerable clinical
50 burden, as the majority of patients are diagnosed at advanced stages or progress to metastatic
51 disease after initial treatment[3]. The 5-year overall survival (OS) rate for patients with metastatic
52 disease is less than 15% [4, 5]. Similarly, PDAC is an aggressive cancer characterized by rapid
53 disease progression, early metastasis, and limited response to conventional therapies[6]. The 5-year
54 OS rate for PDAC for all stages combined remains under 10% despite the use of multi-agent
55 chemotherapy regimens [6, 7]. For patients with chemotherapy-refractory CRC or PDAC, there are
56 currently no FDA-approved therapies that extend overall survival beyond 3 months[5, 7]. These
57 poor clinical outcomes argue for more effective therapeutic strategies that target the molecular
58 vulnerabilities of these cancers.

59 The tumor suppressor *TP53* gene is mutated in most cancers, including CRC and PDAC, and
60 mutant p53 (p53mut) contributes to cancer progression and poor response to therapy[8, 9]. The p53
61 protein is critical for maintenance of genomic stability by regulating DNA repair and cell cycle
62 control at the G1/S checkpoint in response to DNA damage[10]. Despite ample knowledge on the
63 functional consequences of p53 mutations, therapeutic approaches targeting p53mut cancers
64 have been largely unsuccessful, and the p53 status is largely ignored in the clinical management
65 of patients[11]. Cancer cells with mutant p53 show a greater reliance on the G2 checkpoint due to
66 loss of G1-checkpoint control. This vulnerability of p53mut tumors has been explored with
67 agents targeting the G2 checkpoint alone or in combination with chemotherapeutics, such as
68 doxorubicin and carboplatin[12-14]. The major limitations of these approaches are the low

69 selectivity of these therapeutics for p53 status and high hematologic and organ toxicities in
70 combination therapy[15, 16]. The therapeutic strategies with enhanced selectivity towards p53mut
71 cancers are needed to improve treatments of these malignancies [10].

72 Recently, we developed a two-drug therapeutic strategy that induces DNA damage
73 selectively in p53mut cancer cells [17, 18]. This strategy combines a thymidine analogue TAS102,
74 acting as an inducer of DNA single-strand breaks (SSBs) through post-replicative DNA repair,
75 and PARP inhibitor (PARPi) which acts as an amplifier of DNA damage by converting SSBs to
76 more lethal double-strand DNA breaks (DSBs)[17, 18]. The TAS102-PARPi treatment induces G1-
77 arrest in wild-type p53 (p53WT) cells, while p53mut cells exhibit high DSB levels, G2-arrest,
78 and increased cell death [18]. The inducer-amplifier strategy showed greater efficacy in p53mut
79 cancer models, including CRC and PDAC, compared to either drug alone, while no major
80 toxicities were observed in mice [17, 18]. This two-drug strategy is being tested in a first-in-human
81 Phase I clinical trial for patients with refractory CRC using the TAS102-talazoparib combination
82 (NCT04511039)[19]. The preliminary data showed no significant signs of toxicity and improved
83 median progression-free survival (mPFS) compared to historical mPFS for TAS102 alone[19].

84 Here, we show that TAS102-PARPi treatment induces prolonged G2-arrest in p53mut cancer
85 cells even after drug washout, while non-tumor p53WT cells rapidly repair their DNA and
86 reenter the cell cycle. The ATR-WEE1 signaling axis is critical for G2-arrest in response to
87 TAS102-PARPi in p53mut cancer cells. Following TAS102-PARPi treatment, a selective
88 inhibitor of WEE1 kinase releases p53mut cells with unrepaired DNA into mitosis, leading to
89 cell death. This sequential approach combining TAS102-PARPi treatment with a WEE1 inhibitor
90 showed greater tumor control in preclinical models compared to either treatment alone. The
91 sequential triple-drug regimen was well-tolerated in animals even after extended administration.

92 **MATERIALS AND METHODS**

93 **Cell culture models**

94 Human CRC cell lines HT29 (RRID:CVCL_0320) and DLD1 (RRID:CVCL_0248); human non-
95 tumor breast epithelial MCF10A (RRID: CVCL_0598), human breast cancer MDA-MB-231
96 (RRID:CVCL_0062) were obtained from American Type Culture Collection (ATCC, Manassas,
97 VA, USA) and cultured as recommended by ATCC. Human CRC cell lines HCT116, HCT116-
98 p53(-/-; KO), and HCT116-p53(R248W/-), SW48, SW48-p53(-/-; KO) were from Dr. Bert
99 Vogelstein, Johns Hopkins University. Human CRC RKO and RKO-p53(-/-, KO) cell lines were
100 from Dr. Alessandro Carugo, IRBM European School of Molecular Medicine, Italia. The
101 genetics information details for the cell line and PDX models are presented in **Key Resources**
102 **Table**. All human cell lines were authenticated using short tandem repeat profiling by ATCC or
103 the Roswell Park Genomic Shared Resource within the last three years. The cells were routinely
104 screened for mycoplasma, and all studies made use of mycoplasma-free cells. Cell cultures were
105 maintained in media and incubated as recommended by ATCC.

106 **Xenograft animal models**

107 Female SCID/CB17 mice (6-7-week-old) were obtained from a colony of SCID/CB17 mice bred
108 and maintained at the Animal Facility of the Roswell Park Comprehensive Cancer Center.
109 Pancreatic patient derived xenografts (Panc-PDX-14312-4p) were implanted sc into SCID mice,
110 while colorectal patient derived xenografts (CRC PDX-3B1-29-3p) were grown in NOD.Cg-
111 Prkdc^{scid} Il2rg^{tm1Wjl}/SzJ mice (Jackson Laboratory, Bar Harbor, ME), also known as NOD SCID
112 gamma (NSG). Animals were kept in microinsulator units and provided with food and water *ad*
113 *libitum* according to a protocol and guidelines approved by the Institute Animal Care and Use
114 Committee (IACUC). The facility is certified by the American Association for Accreditation of
115 Laboratory Animal Care (AAALAC) and in accordance with current regulation and standards of
116 the US Department of Agriculture and the US Department of Health and Human Services.

117

118 **Cell-derived xenografts in mice**

119 Female SCID/CB17 mice (6−8-week-old) were obtained from a colony of SCID/CB17 mice bred
120 and maintained at the Animal Facility of the Roswell Park Comprehensive Cancer Center.
121 Animals were kept in microinsulator units and were provided with food and water *ad libitum*
122 according to a protocol and guidelines approved by the Institute Animal Care and Use
123 Committee (IACUC). The facility is certified by the American Association for Accreditation of
124 Laboratory Animal Care (AAALAC) and is in accordance with current regulations and standards
125 of the US Department of Agriculture and the US Department of Health and Human Services.
126 Mice were inoculated subcutaneously into the left flank with exponentially growing HT29 tumor
127 cells at (1×10^6/mouse). Tumor growth was monitored by measuring tumor diameters with
128 electronic calipers twice/a week. Volumes were calculated using the formula (length) ×
129 $(\text{width})^2/2$. Mouse weights were measured twice/week. Once the tumor volume reached 50-100
130 mm^3, mice were randomly assigned (n = 8-10/group) into four treatment arms: (1) vehicle
131 control, (2) WEE1 inhibitor (WEE1i, adavosertib, MK-1775, 40-60 mg/kg), (3) TAS102-
132 talazoparib (TAS102: 50 mg/kg, talazoparib: 0.150 mg/kg), and (4) sequential regimen
133 (TAS102-talazoparib for one week followed by WEE1i in the second week). TAS102 and
134 talazoparib were dissolved in 12% HPCD (2-hydroxypropyl)-β-cyclodextrin in DPBS, while
135 MK-1775 was prepared in 5% DMSO, 40% PEG300, 5% Tween-80, and 50% saline. All drugs
136 were freshly prepared and administered via oral gavage on a 5-days-on, 2-days-off schedule. At
137 the tumor diameter of $2cm^3$, mice were euthanized and subjected to necropsy and organ
138 collection. Tumor growth assessment was stopped once a mouse reached the endpoint (typically
139 in a vehicle-treated cohort) while the survival data were still collected in the study. Tumor tissues

140 were collected by snap-freezing in liquid nitrogen for RNA and protein analyses. Blood was
141 collected for CBC by cardiac puncture.

142 **Patient Derived Xenograft (PDX)**

143 Donor and experimental pancreatic patient-derived xenografts (PDAC-PDX-14312-4p) were
144 implanted subcutaneously into SCID mice, while colorectal patient-derived xenografts (CRC
145 PDX-3B1-29-RP-3p; APC E1353*, KRAS-G12D, TP53-R213*, PIK3CA-E545K) were grown
146 in NOD-Cg-Prkdcscid Il2rgtm1Wjl/SzJ mice (Jackson Laboratory, Bar Harbor, ME), also known
147 as NOD SCID gamma (NSG). Tumors were grown in donor mice to a volume of ~1500mm^3,
148 harvested rapidly after euthanasia, cut into 2×2×2 mm^3 pieces under sterile conditions, and
149 surgically implanted into the left flank. Surgical staples were removed about ten days post
150 implantation, and tumor growth and mouse weights were measured two times a week. At the
151 average tumor volume of 100mm^3, mice were randomized and treated as described above.

152 **Complete Blood Counts**

153 Blood was collected by cardiac puncture into a tube containing EDTA to prevent coagulation at
154 the endpoint of the study. Analysis was performed using the HemaTrue Analyzer and
155 HeskaView Integrated Software version 2.5.2. The graphs for the blood compounds were
156 generated using GraphPad Prism8 (Version 8.4.2).

157 **Immunoblotting**

158 Whole-cell lysates were prepared using NP40 Lysis Buffer (0.88% NP-40, 132 mM NaCl, 44
159 mM HEPES, and 8.8 mM NaF) supplemented with 2 mM sodium orthovanadate, 1 mM PMSF,
160 and Protease Inhibitor Cocktail. Protein concentrations were quantitated using the Bio-Rad DC
161 Protein Assay (Cat# 5000111). An equal concentration of protein from each sample was
162 calculated, boiled at 100°C for 5 minutes, and resolved by SDS-PAGE at a constant voltage of
163 100V. Proteins were then transferred onto a nitrocellulose membrane (0.2-µm pore size) at a

164 constant voltage of 100V for 120 minutes at 4°C. Membranes were blocked in 1X TBS-T (Tris-
165 buffered saline (TBS) with 0.1% v/v TWEEN-20) and 5% w/v non-fat dry milk. Primary
166 antibodies (listed in Table 2) were diluted in 5% BSA or 5% of milk in 1X TBS-T and incubated
167 overnight at 4°C. The membranes were washed three times with 1X TBST for 10 minutes each,
168 then incubated with secondary mouse or rabbit HRP-conjugated antibody for 1 hour at room
169 temperature (listed in Table 2). The membranes were washed three times with 1X TBST for 15
170 minutes each. Pierce ECL Western Blotting Substrate was used for chemiluminescent detection.
171 Signals were visualized and imaged using radiographic films.

172 **Cell cycle analysis by Flow Cytometry**

173 Cells were seeded at 300,000 cells/well in 6-well plates and then treated with various amounts of
174 talazoparib for 24 h. Collected cells were fixed with ice-cold 70% ethanol for 1 hour at -20°C
175 and stained for 1 hour at 4°C in Krishan DNA Buffer (propidium iodide, sodium citrate, RNase
176 A, NP40, and 0.1 mM HCl). The samples were analyzed on a BD LSR Fortessa cytometer
177 running FACS Diva (Version 6.1.3), and the data were processed using FCS Express 7 (Version
178 7.06.0015). Experiments were repeated twice, and representative histograms are shown.

179 **Cytotoxicity**

180 Cells were seeded at a density of 5,000 cells per well in a 96-well plate. After 24 hours, cells
181 were treated with TAS102 at a range of concentrations in the presence of 100nM talazoparib,
182 and/or the G2 kinase inhibitors at various concentrations for 72 hours. Cells were stained with
183 1% methylene blue for 30 minutes, rinsed with water, and dried overnight. The next day, cells
184 were solubilized in 5% SDS prepared in PBS, and absorbance was measured at 650 nm. IC50
185 values were calculated using GraphPad Prism (Version 10.0.3). Combination Index (CI) values
186 were calculated based on the Loewe Additivity Model as implemented in the SynergyFinder R
187 package using the following formula: $CI = D1/IC50_1 + D2/IC50_2$, where D1 and D2 are the

188 concentrations of drugs 1 and 2 used in the combination, while $IC50_1$ and $IC50_2$ are the
189 concentrations of drugs 1 and 2 inhibiting 50% of the activity when used individually. Each dot
190 in the Scatter plot represents the drug interaction in the combination at specific concentrations,
191 plotted against the fraction affected (Fa). The CI values are distributed below, at, or above the
192 threshold of 1, indicating synergy (CI < 1), additivity (CI = 1), or antagonism (CI > 1).

193 **Immunohistochemistry (IHC)**

194 Freshly isolated tumors were fixed in 10% neutral buffered formalin (Sigma-Aldrich, Cat.
195 #HT501128) for 48 hours, then transferred to 70% ethanol for dehydration, before embedding in
196 paraffin by Roswell Park's Pathology Network Shared Resources (PNSR) into formalin-fixed
197 paraffin-embedded (FFPE) blocks. Staining for hematoxylin & eosin (H&E) and for p-Y15-
198 CDK1, Cyclin B1, and p-S10-HH3 were performed by the PNSR. Antibodies and reagents are
199 listed in **Key Resources Table.** Slides were scanned by Aperio ImageScope version 12.4.0.5043,
200 and representative images were captured at 20x magnification. Three representative tumors from
201 each treatment group were used for quantification. A minimum of eight fields of view (FOV)
202 were analyzed for each tumor sample. Entire stained tissue sections were scanned, and the areas
203 of highest density for immunoreactivity ("hot spots") were manually selected for quantification.
204 Each "hot spot" was recorded at 20x magnification. The positive area was calculated using the
205 formula: Negative area – Positive area × 100) in ImageJ. Data were reported as mean and
206 standard error (mean +- SE). Data were presented using GraphPad Prism8 (Version 8.4.2).

207 **Annexin-V staining**

208 Following drug exposure, cells were trypsinized, washed with PBS, and resuspended
209 in Annexin-binding buffer. Dead cells were stained for annexin-V (surface marker) and DNA
210 with propidium iodide according to the manufacturer's instructions (Dead Cell Apoptosis Kit
211 with Annexin-V-FITC and PI, for flow cytometry, ThermoFisher Scientific, Cat. No.: V13242).

212 The samples were processed on a BD LSR Fortessa cytometer running FACS Diva (Version
213 6.1.3), and the data were analyzed using FCS Express 7 (Version 7.06.0015). Experiments were
214 repeated twice, and representative histograms were shown.

215 **Immunofluorescence microscopy**

216 Cells were grown on glass coverslips for 24 hours and then treated with 500nM TAS102, 100nM
217 talazoparib, or their combination for the indicated time; alternatively, cell were treated with
218 TAS102-talazoparib for 25 hours following drug withdrawal in incubation for indicated time.
219 Cells were fixed with 4% PFA and permeabilized with 0.05% Triton X-100. Samples were
220 blocked with 3% milk in PBS and probed with γH2AX and RAD51 antibodies in 1% milk,
221 followed by a wash in PBS and incubation with fluorescent secondary antibodies in 0.5% milk.
222 Samples were washed with PBS three times and DNA was labeled with Hoechst 33342 before
223 mounting on glass slides. Fluorescence images were taken with a Plan Apochromat 100x
224 objective (1.40 NA mineral oil) at ambient temperature using a Nikon TE2000-E inverted
225 microscope equipped with a charge-coupled device camera (CoolSNAP HQ; Photometrics). The
226 levels of γH2AX and RAD51 were assessed by measuring cellular fluorescence intensity as the
227 Corrected Total Cellular Fluorescence (CTCF). Briefly, a minimum of six random fields per
228 treatment group were evaluated using MetaVue imaging software (Version 7.7.3, Molecular
229 Devices). Three background readings were measured for each field of view and individual cells
230 that were positively stained with γH2AX and RAD51 were selected with a region freehand tool.
231 For each treatment group, >40 cells were evaluated and the CTCF values were calculated using
232 the formula: integrated density – (area of cell × average background fluorescence). The CTCF
233 values were reported as mean and standard error (mean +- SE). Data was presented using
234 GraphPad Prism8 (Version 8.4.2).

235 **RNA sequence**

236 Cells were seeded at a density of $1x10^6$ cells in a 100mm dish, and the following day media was
237 replaced with base media containing 5% FBS for 6 hours. Cells were then treated with 500nM
238 TAS102, 100nM talazoparib or their combination for 24 hours. Next day, cells were lysed with
239 TRIzol reagent (Thermofisher Scientific; Cat # 15596026). RNA was isolated using Direct-zol
240 RNA Miniprep Kit (Zymo Research; Cat # R2050). The sequencing libraries are prepared from
241 500ng total RNA using the mRNA HyperPrep kit (Roche) and following manufacturer's
242 instructions. The polyA+ RNA population was captured using the mRNA Capture Beads and
243 then utilized for cDNA synthesis using random primers and reverse transcriptase. cDNA was
244 converted into blunt-ended double-strand DNA using Taq pol (overhanging A) and purified
245 using Pure Beads (Roche). Multiple indexing adapters with overhanging T at the 3' end were
246 ligated to the ds-cDNA ends. Adapter ligated ds-cDNA libraries were amplified by PCR,
247 purified using Pure Beads, and then were validated for appropriate size on a 4200 TapeStation
248 D1000 Screentape (Agilent Technologies, Inc.). The DNA libraries are quantitated using KAPA
249 Biosystems qPCR kit, and are pooled together in an equimolar ratio, following experimental
250 design criteria. Each pool is denatured and diluted to 200pM with 1% PhiX control library
251 added. The resulting pool is then loaded into the appropriate NovaSeq Reagent cartridge, as
252 determined by the desired sequencing depth and number of samples. 100-cycle paired-end
253 sequencing is then performed on a NovaSeq6000 following the manufacturer's recommended
254 protocol (Illumina Inc.).
255 Raw count files were generated from FASTQ files using UB CCR's HPC nr-core/rnaseq pipeline
256 (https://nf-co.re/rnaseq/3.12.0). Raw sequencing reads passed quality filters from Illumina RTA
257 were first pre-processed by using FASTQC (v0.11.8) for sequencing base quality control. The
258 reads were mapped to GRCh38 human reference genome and the GENCODE (v38) (128)

259 annotation database using STAR (v2.7.9a). Counts from RSEM were filtered and then upper
260 quartile normalized using R package edgeR. Gene Ontology analysis of biological processes
261 pathways was selected based on adjusted p-values, and the NES was calculated by ranking all
262 genes based on their differential expression, calculating the Enrichment Score (ES) for each gene
263 set, and normalizing the ES by dividing it by the mean ES values from random permutations.
264 Cell-cycle genes in the heatmap were derived from the Cyclebase 3.0 database.

265 **Quantification and Statistical Analysis**

266 Statistical analysis was performed using GraphPad Prism software (Version 10.0.3) unless
267 otherwise indicated. The data represent biological replicates (n) as mean value with standard
268 error (mean ± SE). Statistical significance of data comparisons was determined using the
269 Student's unpaired *t*-test with a two-tailed distribution, one way ANOVA, or two-way ANOVA
270 with a Tukey multiple comparisons test or with Sidak's multiple comparisons test as indicated in
271 figure legends. Statistical significance was achieved when $P<0.05$. The correlation analysis was
272 performed using Pearson correlation approach in RStudio. Survival was evaluated using the
273 Kaplan-Meier estimator with the log-rank test, based on time-to-arrive at a defined tumor volume
274 using GraphPad Prism. Cytotoxicity data were normalized to control and IC50 was calculated
275 using three-parameter nonlinear regression.

276

277 **RESULTS**

278 **The TAS102-talazoparib treatment activates DNA damage response and arrests cells in G2.**

279 Prior studies have shown that incorporation into DNA of thymidine analogues (i..e., ethynyl-
280 deoxyuridine, EdU, or trifluorothymidine, a component of TAS102) triggers post-replicative
281 repair that results in single-strand DNA break (SSB) intermediates [17, 18]. Addition of PARP
282 inhibitor (PARPi) greatly increases formation of double-strand breaks (DSBs) [17, 18]. DNA

damage activates p53-dependent G1 checkpoint and DNA repair in non-tumor p53WT cells, whereas p53mut cells (exhibiting a compromised G1 checkpoint) accumulate DSBs and respond with the G2 checkpoint [17, 18]. To define the molecular mechanisms of the G2 checkpoint response to TAS102-PARPi treatment, isogenic CRC cell lines were utilized with p53WT, p53mut or p53-deletion (KO, knockout). Treatment with talazoparib (PARPi) for 24 hours increased the G2 population in p53mut and p53KO cells while had little effects in p53WT cells, whereas TAS102 alone increased the G2 population in p53mut/p53KO cells and a moderate G2 increase in p53WT cells (**Fig. 1a-b**). TAS102-talazoparib treatment (TAS-Tal) exerted in p53mut/p53KO cells a strong increase in the G2 population and a reciprocal decrease in G1-population, and these changes were statistically significant (**Fig.1a-b**). In p53WT cells, the combination did not increase G2-population compared to TAS102 alone. The immunoblot analysis of cell cycle and DNA damage response (DDR) markers showed that TAS102 and TAS102-PARPi decreased an activating phosphorylation of PLK1, a kinase mediating mitotic transition, independent of p53 status (**Fig.1c-d**). The TAS102-PARPi treatment increased an inactivating phosphorylation of CDK1 at Tyr15 (**Fig. 1c-d**), a site known to be phosphorylated by WEE1 kinase. Protein levels of cyclins A2 and B1, partners of CDK1, were also elevated (**Fig.1c-d**). In contrast, phosphorylation of histone H3 was not induced, showing no entry to mitosis (**Fig.1c-d**). Together, these results showed induction of the G2 checkpoint and DDR in p53-deficient cells upon treatment with TAS102 alone and, more robustly, in combination with PARPi (**Fig.1g**). To validate this observation *in vivo*, the G2 markers were examined by immunohistochemistry (IHC) in tumor tissues from the CRC PDX models (generated within the Phase I clinical NCT04511039 study), that were treated with vehicle or the drugs (talazoparib, TAS102, or combination) as described [18]. The IHC analysis showed that TAS102 and TAS102-PARPi

306 increased levels of phospho-Tyr15-CDK1 and Cyclin B1 in $p53^{H179R}$ mutant model (PDX-02-07-
307 RP), whereas levels of phospho-H3 were reduced (**Fig. 1e** and **Suppl. Fig.1a-b**). Similar results
308 were obtained using PDX-01-03-RP model carrying p53WT, although the effects of the drug
309 combination were lower in the p53WT model (**Fig. 1f** and **Suppl. Fig.1c-d**). These findings
310 indicate that the TAS102-PARPi combination primarily activated the G2 checkpoint in p53mut
311 cancers, while p53WT cells respond with activation of both G1 and G2 checkpoints (**Fig. 1g)**.
312

313 **TAS102-talazporib alters the transcriptomic program in p53WT and p53mut cells.**

314 To better define the response to the two-drug combination, the transcriptomic analysis was
315 performed on isogenic HCT116 p53WT and p53KO cell lines treated with drug monotherapies
316 or their combination for 24 hours. Talazoparib alone induced minimal transcriptomic changes in
317 both cell lines (**Fig. 2a, d**). In contrast, TAS102 exerted strong effects by inducing expression of
318 774 genes and downregulating expression of 367 genes in p53WT cells and 614 upregulated and
319 418 downregulated genes in p53KO cells relative to vehicle-treated controls (**Fig. 2b, e**). The
320 drug combination in p53WT cells increased expression of 897 genes and decreased expression of
321 368 genes, while in p53KO cells expression of 698 genes was induced and for 615 genes was
322 decreased (**Fig. 2d, f**). The Venn diagrams demonstrated a notable overlap in altered gene
323 expression between TAS102 monotherapy and the TAS102-PARPi combination, with 936 shared
324 in p53WT and 770 shared in p53KO cells (**Fig. 2g-h**).

325 To infer the biological processes affected by the drug treatments, the gene ontology (GO)
326 enrichment analysis was conducted on the differentially expressed genes (**DEGs**). The GO
327 analysis showed that in both p53WT and p53KO cells treated with TAS102, the up-regulated
328 genes were enriched in processes associated with cell cycle regulation and extracellular matrix

329 (ECM) organization (**Suppl. Fig. 2a-b**). However, among the down-regulated genes distinct
330 processes were affected in p53WT *vs*. p53KO cells. In p53WT cells, the down-regulated genes
331 were mainly associated with processes related to mRNA splicing and pyrimidine metabolism,
332 whereas in p53KO cells with processes related to ribosome biogenesis, rRNA processing and
333 maturation (**Suppl. Fig. 2a-b**). In TAS102-talazoparib treatment, the top upregulated biological
334 processes in p53KO cells were related to DNA replication and the G2/M transition, while
335 downregulated processes were related to ribosome biogenesis (**Suppl. Fig. 2c-d**). The dot plots
336 summarize the top significantly enriched processes related to cell cycle regulation, ECM
337 organization, and ribosome biogenesis for p53WT and p53KO cells (**Fig. 2i**). The upregulation
338 of processes related to ECM organization suggests a contribution of matrix to cell division, while
339 repression of ribosome biogenesis is consistent with a reduced ribosome biogenesis at the G2
340 checkpoint in preparation for mitosis [20].

341 To reveal the response differences related to cell cycle and DNA repair in p53WT *vs*. p53KO
342 cells, the heatmaps were built for p53 targets, cell cycle, and DNA repair genes identified in the
343 GO analysis. The regulation of p53 target genes was clearly different between p53WT and
344 p53KO cells (**Fig. 2j, k**). Treatment of p53WT cells with TAS102 (TAS) or TAS102-PARPi
345 (TAS+Tal) strongly induced the expression of p53 targets (i.e., p21/CDKN1A, MDM2, BTG2),
346 in contrast their regulation was markedly lower in p53KO cells (**Fig. 2j, k**, p53 Targets). In
347 p53KO cells the expression of homologous recombination (HR) DNA repair genes (i.e., BRCA1,
348 BRCA2, RAD51) was robustly induced by TAS102-PARPi treatment, while the effect was lower
349 in TAS102 alone (**Fig. 2j, l**, HR genes). This finding is consistent with higher double-strand
350 breaks (DSBs) induced by TAS102-PARPi treatment in p53KO cells compared to TAS102 alone
351 [17, 18]. The genes involved in G1/S transition (CDK4, E2F1, E2F3) and DNA replication (MCM6,

352 PRIM2) were reduced in p53WT cells treated with TAS102 and TAS102-PARPi (**Fig. 2j, m**). In
353 contrast, treatment of p53KO cells with TAS102 or TAS-PARPi increased expression of genes
354 mediating G1->S transition (E2F1, E2F3, TFDP1) and DNA replication (CCNE1, CDK2,
355 MCM10, ORC1), **Fig. 2j, m**, G1/S and S/G2 genes. These effects show that neither TAS102 nor
356 TAS-PARPi repress DNA replication in p53-deficient cells, whereas the treatments of p53WT
357 cells induce a p53-dependent G1-arrest. Importantly, treatment with TAS-PARPi of p53KO cells
358 strongly reduced expression of genes involved in mitosis (AURKA, BUB1, CDC20, CENPF,
359 PLK1, PIF1), an effect that was lower in TAS102 alone (**Fig. 2j**, **n**, M phase). In contrast, the
360 expression of these genes was not reduced in p53WT cells. We further verify the transcriptome
361 effects in the HT29 CRC cell line carrying mutant $p53^{R273H}$. The RNAseq analysis showed that
362 TAS102-PARPi treatment downregulates expression of M-phase genes and upregulates
363 expression of HR-related genes comparable to the effects observed in HCT116-p53KO cells
364 (**Suppl. Fig. 3**). The TAS102-PARPi effects were greater than those exerted by TAS102 alone.
365 Together, these data showed the TAS102-PARPi treatment causes distinct transcriptome changes
366 in p53-deficient *vs*. p53WT cells, consistent with G2-arrest and activation of HR-mediated DSB
367 repair in p53mut cells, but G1-arrest in p53WT cells.
368

369 **Targeting G2 checkpoint kinases and cytotoxicity of TAS102-PARPi treatment.**

370 We have shown that TAS102-PAPRi treatment activates signaling by ATM and ATR kinases
371 [18], which are known to mediate DNA repair and G2-arrest [21, 22]. Therefore, we examined whether
372 blockade of these kinases can enhance the toxicity of TAS102-PARPi in p53mut cells. Selective
373 ATM inhibitor (KU55933; ATMi) did not enhance toxicity of TAS102-talazoparib in p53WT
374 and p53-deficient (p53KO, $p53^{R248W/-}$) HCT116 cell lines (**Suppl. Fig. 4a-c**). Instead, ATMi

375 reduced sensitivity to TAS102-talazoparib in all tested lines, potentially due to ATM function in
376 the G1/S checkpoint [23] and/or recovery of replication fork after DNA repair [21, 22]. In contrast, the
377 selective ATR inhibitor (AZD6738/ceralasertib; ATRi) markedly enhanced toxicity of TAS102-
378 talazoparib in p53KO and p53mut cell lines (**Fig. 3a-d**). In p53-deficient cells the IC50 was
379 enhanced 4-10-fold by 100nM ATRi (**Fig. 3b-d, n**), whereas only 1.5-fold increase was observed
380 in p53WT cells (**Fig. 3a, n**). This result is consistent with our prior finding that, in cells treated
381 with TAS102-talazoparib, blockade of ATR increases levels of γH2AX (a DNA damage marker)
382 [18]. Further, blockade of ATR, but not ATM, increased phosphorylation of histone H3 (phospho-
383 H3, a marker of mitosis) (**Suppl. Fig.4i**). These data are aligned with the role of ATR in
384 resolving replication stress and activating the G2/M checkpoint, thus ensuring proper cell cycle
385 progression and DNA repair [24]. Blockade of ATR kinase allows cells with unrepaired DSBs to
386 enter mitosis, leading to cell death [22].

387 ATR kinase induces G2-checkpoint through downstream effector kinases such as CHK1 and
388 WEE1; CHK1 kinase phosphorylates and inactivates CDC25 phosphatase, which controls
389 CDK1, while WEE1 kinase inactivates CDK1 by phosphorylating Tyr15 [21, 25-30]. Therefore, we
390 explored whether blockade of these kinases will result in cytotoxic effects comparable to ATRi.
391 Selective CHK1 inhibitor (AZD7762; CHK1i) showed comparable increase in cytotoxicity of
392 TAS102-talazoparib in both p53WT and p53-deficient cells, about 8-10-fold at 100nM CHK1i
393 (**Fig. 3e-i**). In contrast, a WEE1 inhibitor (MK1775; WEE1i) enhanced the cytotoxicity of
394 TAS102-talazoparib preferentially in p53mut cells, 8-15-fold in p53mut *vs* 3-4-fold in p53WT
395 cells at 100nM WEE1i (**Fig. 3j-m, o**).

396 Next, we examined the cytotoxicity of G2-kinase inhibitors in non-tumor p53WT MCF10A
397 cells. ATRi and WEE1i showed only a moderate (2-3-fold) enhancement of toxicity of TAS102-

398 talazoparib in non-tumor cells (**Suppl. Fig. 4d, f**). In contrast, CHK1i strongly enhanced toxicity
399 of TAS102-talazoparib (nearly 10-fold) in non-tumor cells (**Suppl. Fig. 4e**). Immunoblotting
400 verified the activities of CHK1 and WEE1 inhibitors on DNA damage response (DDR) markers
401 in p53WT MCF10A and p53mut MDA-MB-231 cells (**Suppl. Fig. 4g, h**). Consistent with the
402 effects of CHK1i *in vitro*, clinical trials have shown significant toxicities associated with CHK1i,
403 resulting in discontinued early trials [31, 32]. Conversely, drugs targeting ATR and WEE1 have
404 shown tolerable toxicity in clinical trials [33, 34], positioning them as potential therapeutic
405 candidates. Given that both ATRi and WEE1i enhanced efficacy of TAS102-talazoparib
406 preferentially in p53mut cells, we evaluated the drug interaction using the Loewe Additivity
407 Model [35, 36]. The analysis revealed synergism of TAS102-talazoparib with both ATRi and
408 WEE1i in p53mut cell models, with cooperativity index (CI) values ranging from 0.21 to 0.30
409 for ATRi (**Fig. 3n**, **Suppl. Fig. 5a-d**) and 0.16-0.30 for WEE1i (**Fig.3o**, **Suppl. Fig. 5f-i**). In
410 contrast, in non-tumor p53WT cells, ATRi and WEE1i did not show substantial cooperativity
411 with TAS102-talazoparib with the CI values of 0.73 and 0.69, respectively (**Fig. 3n-o** and **Suppl.**
412 **Fig. 5e, j**). Thus, in this simultaneous drug regimen, TAS102-talazoparib synergized in
413 cytotoxicity with ATRi and WEE1i in p53mut cancer cells, while exerting only moderate
414 interaction in p53WT cells.
415

416 **TAS102-talazoparib induces persistent DNA damage in p53-mutant cancer cell models.**

417 A clinical drug regimen for TAS102 and TAS102-talazoparib includes cycles of 5-days On-
418 treatment plus a 9-day Off period [37]. To explore the response dynamics, the cell-cycle analysis
419 was performed on p53WT and p53-deficient cells treated with TAS102-talazoparib followed by
420 drug washout. In p53WT cells, an increase in the G2 population was observed following the two-

421 drug treatment and remained elevated up to 24 hours after drug washout, then followed by a
422 gradual increase in the G1 population, with a small fraction of sub-G1 cells (**Fig. 4a**). In contrast,
423 p53KO and p53R248W cells responded to TAS102-talazoparib with a prolonged G2-arrest even
424 after drug withdrawal. Moreover, the sub-G1 population was increased at 48-72 hours after drug
425 withdrawal, indicating cell death in p53-deficient cells (**Fig. 4b-c**).

426 To verify the cell cycle effects and to assess DNA damage, the molecular markers of DDR
427 and cell cycle were examined by immunoblotting in cells treated with TAS102-talazoparib for
428 24hours followed by drug washout. In HCT116-p53WT cells, 24hr-treatment with TAS102-
429 talazoparib (T0) induced the markers of G2-checkpoint (phospho-CHK1 and phospho-CDK1)
430 and DNA damage (γH2AX) (**Fig. 4d**). The levels of these markers decreased after 24hours of
431 drug washout. Protein levels of p21/CDKN1A (a p53 target) followed this trend with a reduction
432 at 36hours (**Fig. 4d**). Cyclin D1 levels increased at 36hours, indicating a recovery of cell cycle
433 capacity (**Fig. 4d**). Together, these findings align with the cell cycle data (**Fig. 4a**). In contrast,
434 HCT116-p53KO and HCT116-p53$^{R248W/-}$ cells exhibited sustained phospho-CHK1, phospho-
435 CDK1, and γH2AX levels after the TAS102-talazoparib treatment, indicating a prolonged G2-
436 arrest with high DNA damage (**Fig. 4e-f**). In support, cyclin D1 protein levels remained low, not
437 recovering within 72 hours (**Fig. 4e-f**). Comparable results were observed in HT29-p53^{R273H} cells
438 (**Fig. 4g**), where a prolonged increase in DNA damage and G2 markers mirrored the data in
439 HCT116 p53KO and p53R248W/- cell lines.

440 To validate the recovery of cell proliferation following treatment with TAS102-talazoparib
441 for 24hours and drug withdrawal, cell growth was examined using live-cell imaging. The
442 analysis showed that p53WT non-tumor MCF10A cells quickly recovered growth capacity after
443 drug washout, while growth recovery was delayed by ~48hours in p53WT HCT116 cells (**Suppl.**

444 **Fig. 6a, b**). In contrast, p53KO and p53mut cancer cells did not regain the growth capacity
445 within the 92hr timeframe of the experiment (**Suppl. Fig. 6c-d**).
446 Together these data showed that TAS102-talazoparib induced in p53-deficient cells a long
447 G2-arrest and persistent DNA damage observed even after 72hours of drug withdrawal, and a
448 sizable proportion of p53mut cells underwent cell death within 48-72hours (sub-G1 fraction). In
449 contrast, p53WT cells were able to repair DNA and recover the cell cycle capacity within
450 48hours of drug withdrawal.
451
452 **The dynamics of DNA repair following TAS102-talazoparib treatment in p53mut cells**
453 To evaluate the dynamics of DNA damage repair, changes in DSB markers γH2AX and
454 RAD51 were examined in MCF10A (p53WT), DLD1 ($p53^{S241F}$), and HT29 ($p53^{R273H}$) cell lines
455 using immunofluorescence. Cells were treated with TAS102-talazoparib for 24hours followed by
456 drug washout. Immediately after 24hr-treatment (at T0), the levels and the foci formation of
457 γH2AX and RAD51 were increased in all tested cell lines (**Fig. 5a, d, e, g, j, k, m, n**). In
458 MCF10A cells, the nuclear area was increased by nearly 2-fold (from 130μm^2 to 250μm^2)
459 (**Fig.5c, f**), indicating enlargement of the nucleus in a significant proportion of cells (about 77%
460 with area of 200-580μm^2, insert). Following drug withdrawal, the γH2AX and RAD51 signals
461 and the nuclear sizes were decreased within 24-48 hours in MCF10A cells (**Figs. 5c-f**). These
462 data show that DNA damage by TAS102-talazoparib was repaired, and cells completed the
463 mitotic cell division. In contrast, the γH2AX/RAD51 signals were not reduced in p53mut DLD1
464 and HT29 cell lines within 72 hours of drug washout (**Fig. 5g-h, j-k, m-n**). The nuclear area was
465 also increased at T0, and a sustained enlargement was observed at 24-48 hours of drug washout
466 (**Fig. 5i, l, o**). These results indicate that p53mut cells replicate DNA but do not undergo cell

467 division resulting in enlarged nucleus, and DSBs are not repaired up to 72hours of drug washout.
468 Together, these observations show that the TAS102-PARPi treatment can induce DNA breaks
469 and G2-arrest in p53WT and p53mut cells. However, DNA repair and recovery of cell division
470 were remarkably different in p53WT and p53mut cells. Non-tumor p53WT cells repaired DNA
471 breaks and completed the mitotic cell division within 48hours, whereas p53mut cells could not
472 complete DNA repair and cell division, resulting in high levels of DNA breaks and G2-arrest
473 even at 72hours of drug withdrawal. These observations are aligned with the cell cycle and cell
474 growth data, which showed a lack of proliferation in p53mut cells within this timeframe (**Fig. 4,**
475 **and Suppl. Fig.5**). Thus, TAS102-PARPi treatment induced high DSB levels and long G2-arrest
476 in p53mut cancer cells, while p53WT cells repaired DNA and recovered cell cycle capacity.
477

478 **A sequential triple-drug approach using TAS102-PARPi treatment followed by blockade of**
479 **WEE1 kinase elicits synergistic toxicity in p53mut cancer cells.**

480 TAS102-PARPi treatment induced DNA breaks and sustained G2-arrest in p53mut cells even
481 after drug washout, whereas non-tumor p53WT cells recovered remarkably faster (**Figs. 4-5**).
482 Next, we examined whether toxicity of TAS102-PARPi treatment in p53mut cells can be further
483 enhanced by blockade of a G2-checkpoint kinase. Cells were treated with TAS102-talazoparib
484 for 24 hours, followed by drug washout for 24 hours and subsequent incubation with WEE1i
485 (MK1775) for 48 hours. Cytotoxicity assays showed that WEE1i did not synergize with
486 TAS102-PARPi in p53WT MCF10A cells, ~1.1-fold at 100nM WEE1i (**Fig. 6a, f**). In HCT116-
487 p53WT cells, WEE1i only modestly enhanced the IC50 of TAS102-talazoparib (by ~1.4-fold at
488 100nM WEE1i). In contrast, in HCT116-p53KO and HCT116-p53^{R248W} cell lines WEE1i at
489 100nM enhanced toxicity of TAS102-talazoparib by ~3.6-fold and ~2.5-fold, respectively (**Fig.**

490 **6b-d, f**). In HT29 ($p53^{R273H}$) cells, the toxicity of TAS102-talazoparib was enhanced by ~7-fold
491 at 100nM WEE1i (**Fig. 6e-f**). Evaluation of drug interactions in this sequential regimen showed
492 CI = 0.94 for MCF10A cells and CI = 0.57 for HCT116 cells (both p53WT), indicating no or
493 modest drug interactions, respectively (**Fig. 6f**). In contrast, p53-deficient cells, HCT116-p53KO
494 or p53mut cells (HCT116-$p53^{R248W}$ and HT29-$p53^{R273H}$), showed CI values ranging 0.26-0.42,
495 indicating a synergistic interaction between TAS102-talazoparib and WEE1i (**Fig. 6f**).
496 Examination of cell death, using flow cytometry with Annexin V and propidium iodide (PI)
497 staining, showed that the sequential treatment of MCF10A cells with TAS102-PARPi followed
498 by 100nM WEE1i resulted in ~9% of double-positive (annexin-V^+/PI^+) dead cells, compared to
499 ~8% dead cells by TAS102-PARPi treatment alone (**Fig. 6g-h**). In HCT116-p53WT cells, ~19%
500 of cells were double-positive after TAS102-talazoparib treatment and ~39% after the sequential
501 triple-drug combination (**Fig. 6g, i**). Approximately 29% of HCT116-p53KO cells were double-
502 positive in response to TAS102-talazoparib, and cell death was increased to ~68% after the
503 triple-drug treatment (**Fig. 6g, j**). In HT29 cells, treatment with TAS102-talazoparib resulted in
504 ~30% double-positive cells, whereas the sequential drug combination resulted in ~76% double-
505 positive dead cells (**Fig. 6g, k**). Similar effects of a sequential triple-drug treatment were
506 observed in p53mut MDA-MB-231 cells compared to p53WT MCF10A cells (**Suppl. Fig. 7**).
507 Together, these data showed a synergistic toxicity of TAS102-talazoparib treatment followed by
508 WEE1i in p53mut cancer cells, whereas this sequential triple-drug regimen showed low toxicity
509 in non-tumor p53WT cells.
510
511 **Anti-tumor efficacy of the sequential triple-drug combination**

512 The therapeutic efficacy of the sequential combination of TAS102-talazoparib and WEE1i
513 was examined in tumor xenograft models. The drug regimen included repeats of the two-week
514 cycle with TAS102-talazoparib treatment in the first week followed by WEE1i treatment in the
515 second week, based on the clinical schedule for TAS102 and TAS102-talazoparib [37]. This two-
516 week regimen was initially tested in xenografts of HT29 cells ($p53^{R273H}$, $BRAF^{V600E}$) in SCID
517 mice. Treatment was initiated when tumors reached $100mm^3$ using 5-days-ON, 2-days-OFF
518 schedule in four groups: vehicle, WEE1i (every week), TAS102-talazoparib (every week), and
519 the triple-drug combination (a sequential two-week cycle). Treatment with WEE1i showed a
520 limited effect on tumor growth with tumor growth inhibition (TGI) of 18%, whereas TAS102-
521 talazoparib was more effective with TGI of 43% (**Fig. 7a-b**), consistent with our previous
522 studies[18]. Importantly, a sequential combination of TAS102-talazoparib and WEE1i showed
523 greater tumor growth control compared to each treatment alone, with TGI of 63% (**Fig. 7a-b**).
524 The triple-drug regimen also improved survival to 39 days compared to 32 days for TAS102-
525 talazoparib, and 24 days for WEE1i alone (**Fig. 7c**). Neither of the treatments affected animal
526 weights compared to the control group (**Fig.7d**), indicating the absence of major toxic side
527 effects.

528 The efficacy of the triple-drug regimen was next tested in a patient-derived xenograft (PDX)
529 model (PDX-3B1-29-RP; $p53^{R213*}$) established from a colorectal cancer biopsy within a clinical
530 trial NCT04511039. The R213* truncating p53 mutation is commonly found in human tumors
531 and exhibits pro-tumor effects [38]. Treatment with TAS102-talazoparib reduced tumor growth by
532 ~20% and WEEi1 alone had no effect, whereas the sequential drug combination reduced tumor
533 growth by ~50% (**Fig. 7e-f**) and extended survival from 24 to 43 days (**Fig. 7g**). No major toxic
534 side effects by the treatments were noted based on examination of mouse weights (**Fig.7h**), the

535 bone marrow histology, and peripheral cell blood counts (**Suppl. Fig. 8**). The efficacy was
536 further examined in pancreatic cancer PDX model (PDX-14312-5p) carrying $p53^{R175H}$ and
537 $KRAS^{G12R}$ mutations. It was observed that WEE1i monotherapy modestly reduced tumor growth
538 (~30%), whereas TAS102-talazoparib was more effective in tumor control with TGI of ~43% at
539 day 50 (**Fig.7i-j**). The triple-drug regimen showed remarkably greater tumor control than either
540 treatment alone (TGI ~80%, **Fig.7i-j**) and extended survival to >75days, compared to ~64 days
541 by TAS102-talazoparib and 48 days by WEE1i (**Fig.7k**). No major toxicity signs were noted
542 based on mouse weights (**Fig.7l**). Together, these data demonstrated that the triple-drug regimen
543 combining the two-drug TAS102-PARPi treatment followed by WEE1i is effective against
544 p53mut cancer models and the regimen is well-tolerated in mice.
545

546 **DISCUSSION**

547 Treatment of p53mut cancers remains a significant clinical challenge mainly due to lack of
548 effective therapeutic options [9, 10]. Here, we introduce a triple-drug strategy for p53mut cancers
549 combining two-drug TAS102-PARPi treatment with blockade of the G2-checkpoint. TAS102-
550 PARPi treatment acts as an *inducer-amplifier* pair to induce DNA double-strand breaks (DSBs)
551 and G2-arrest selectively in p53mut cancer cells. Subsequent blockade of the G2-checkpoint
552 kinase WEE1 releases G2-arrested cells into mitosis leading to cell death, acting as a *terminator*.
553 We found that delaying WEE1i application until after TAS102-PARPi treatment allows normal
554 p53WT cells to repair their DNA, thus reducing the impact on normal cells (**Figs. 5-6**). This
555 sequential triple-drug approach is a promising therapeutic strategy for treatment of p53mut
556 cancers as it showed high efficacy in preclinical cancer models and was well-tolerated in mice.

557 Prior work has shown that TAS102-PARPi treatment induces high levels of DNA damage in
558 p53mut cells selectively, and this effect was linked to a compromised G1/S checkpoint [17, 18].
559 Thymidine (dT) analogues, such as trifluorothymidine (TFT, a component of TAS102) or
560 ethynyl-deoxyuridine (EdU), are incorporated into DNA during replication[17, 18]. These dT-
561 analogues also inhibit thymidylate synthase[39], leading to the incorporation of uridine residues
562 into DNA[17, 18, 40]. The incorporated analogues are removed from DNA by base-excision repair
563 (BER) resulting in single-strand breaks (SSBs) [17, 18, 40], which are repaired *via* a mechanism
564 involving PARP1[41]. PARP1 inhibitors (such as talazoparib) compromise SSB repair, increasing
565 levels of more lethal DSBs that further activate DDR signaling mediated by ATM and ATR
566 kinases. In p53WT cells, DDR signaling mediated by ATM activates the p53-p21 axis resulting
567 in G1-checkpoint activation [18]. p21/CDKN1A inhibits CDK2 and CDK4/6 leading to cell cycle
568 arrest in G1/S and/or inhibit CDK1-cyclin B1 contributing to G2-arrest [42-44]. This effect of
569 TAS102-PARPi treatment is consistent with the role of ATM-CHK2-p53 signaling in DNA
570 damage response [42, 43]. In p53mut cells with compromised G1/S checkpoint, TAS102-PARPi
571 treatment resulted in activation of the G2-checkpoint mediated by ATR and G2-arrest with high
572 DSBs (this study and [18]).
573 The distinct effects of TAS102-PARPi treatment in p53WT and p53-deficient cells are also
574 reflected in the transcriptomic program. In p53WT cells, TAS102-PARPi reduced expression of
575 genes involved in the G1/S transition (e.g., E2F1, E2F3), indicative of G1-arrest. However, in
576 p53-deficient cells, TAS102-PARPi increased expression of the G1/S transition factors (E2F1,
577 E2F3) and S/G2-phase genes (e.g., CCNE1, CCNE2, CDT1), consistent with the lack of G1/S
578 checkpoint in these cells. Moreover, TAS102-PARPi treatment reduced expression of M-phase
579 genes (i.e., AURKA, BUB1, CDC20, PLK1), consistent with G2-arrest in p53-deficient cells.

580 Thus, TAS102-PARPi treatment exhibits the distinct effects on p53WT and p53mut cells in the
581 global expression of genes related to the cell cycle control.
582 The transcriptome analysis also revealed a striking upregulation of HR-related DSB repair
583 genes (BRCA1, BRCA2, RAD51, RECQL, RBBP6) in p53-deficient cells. This distinct effect of
584 TAS102-PARPi treatment is likely to reflect DNA repair at the G2-checkpoint controlled by
585 ATR kinase [45]. In addition, ATM may also contribute to DNA repair by acting through H2AX
586 (γH2AX), RAD51, and BRCA1/2, thus promoting homologous recombination (HR) [46-48]. Thus,
587 in addition to G2-arrest, TAS102-PARPi treatment upregulates HR-mediated DNA repair.
588 Cytotoxicity studies showed a substantial dichotomy in the consequences of ATM and ATR
589 inhibition. Blockade of ATM reduced sensitivity to TAS102-talazoparib treatment in all tested
590 lines cells, independent of the p53 status. This effect of ATM blockade is likely related to the
591 function of ATM in the G1/S checkpoint [23] or replication fork recovery after DNA repair [21, 22]. In
592 contrast, ATR blockade greatly enhanced cytotoxicity of TAS102-talazoparib in p53mut cells,
593 and this effect is related to transition to mitosis with high DNA damage (elevated phospho-H3
594 and γH2AX levels). These results are consistent with the role of ATR in activation of the G2/M
595 checkpoint and in the control of replication completion before mitosis [24]. ATR can also control
596 an intrinsic S/G2 checkpoint, and the ATR blockade may deregulate the S/G2 transition allowing
597 early mitosis with under-replicated DNA and DNA damage [45]. Thus, ATR plays a critical role in
598 activation and control of the G2-checkpoint in p53mut cells treated with TAS102-PARPi,
599 making ATR a potential target to further enhance efficacy of TAS102-PARPi treatment.
600 To induce the G2 checkpoint, ATR activates downstream effector kinases, such as CHK1
601 and WEE1, that inactivate the CDC25-CDK1 axis that controls transition to mitosis [21, 25-30]. Here,
602 we found that CHK1 blockade in combination with TAS102-PARPi treatment was cytotoxic in

603 both non-tumor p53WT and p53mut cancer cells (**Fig. 3**). This effect may reflect CHK1 role in
604 S-phase and explain high toxicities of CHK1 inhibitors observed in clinical trials, leading to
605 discontinuation of early trials [31, 32]. In contrast, WEE1 blockade enhanced toxicity of TAS102-
606 talazoparib preferentially in p53mut cells, while having a limited toxicity in non-tumor models
607 (**Fig.3**). This effect is consistent with tolerable toxicities of WEE1i observed in early-phase
608 clinical trials [33, 34].

609 The drug response studies showed that the selectivity and efficacy of the drug combinations
610 can be enhanced in a sequential triple-drug regimen. TAS102-talazoparib treatment of p53mut
611 cancer cells resulted in prolonged G2-arrest and persistent DNA damage even at 72hours after
612 drug washout with a sizable amount of cell death (**Figs.4-5**). In contrast, p53WT cells were able
613 to repair DNA and re-enter the cell cycle within 48hours of drug withdrawal. Moreover, a 24hr-
614 delay in WEE1i treatment after TAS102-talazoparib washout was still highly effective against
615 p53mut cells but was markedly less toxic to normal cells (**Fig.6**). This sequential triple-drug
616 regimen (TAS102-talazoparib plus 24hr-delayed WEE1i) resulted in massive 80% cell death in
617 p53mut cancer cells, whereas cell death was not increased in non-tumor cells.

618 A sequential triple-drug regimen combining TAS102-talazoparib and WEE1i showed robust
619 anti-tumor effects in preclinical animal models (**Fig. 7**). Tumor growth was reduced by 63% in
620 the CRC HT29 tumor model and ~80% in the PDAC PDX-14312 model ($p53^{R175H}$) (**Fig.7**).
621 Further, the triple-drug treatment was also highly effective in reducing tumor growth in CRC
622 PDX model (~55%). No major toxic side effects were observed during assessment of mouse
623 weights, bone marrow, and peripheral blood.

624 In summary, this study presents a sequential triple-drug strategy combining the two-drug
625 TAS102-PARPi treatment with delayed application of a G2-kinase inhibitor (WEE1i), which

626 together work as an *inducer-amplifier-terminator trio* (**Fig.7m**). The TAS102-talazoparib
627 regimen was well-tolerated in patients with refractory CRC and showed promising median
628 progression-free survival (mPFS) of 5.7 months (NCT04511039) [37]. This study showed that a
629 sequential G2-kinase blockade with WEE1i strongly enhances efficacy of TAS102-talazoparib in
630 p53mut cancers. This sequential triple-drug strategy is a promising approach for management of
631 patients with p53mut cancers.
632

633 **Limitations of the Study**

634 The study demonstrates an increased efficacy of TAS102-PARPi treatment in p53mut CRC and
635 PDAC models. Although, prior work showed that this combination blocks spontaneous breast
636 cancer metastases [17], the current study did not directly assess the effect of the combinatorial drug
637 treatment on metastatic burden (e.g., liver) in PDAC and CRC *in vivo* models. This question will
638 be the subject of future investigations.
639

640 **AUTHOR CONTRIBUTIONS**

641 A.V.B. conceived the idea; A.V.B., R.M.S., J.Z., and M.M.A. designed the experiments; J.Z.,
642 M.M.A., A.V.B, M.N.N and B.G. performed the experiments and analyzed the data; A.V.B. and
643 C.F. analyzed and interpreted the data; T.M. and R.M.S. helped in the interpretation of the data;
644 B.G., B.F., S.C. helped with PDX generation; A.V.B., C.F., T.M., J.Z., M.M.A., R.M.S. and R.I.
645 contributed to preparing and writing the paper.
646

647 **ACKNOWLEDGEMENT**

648 We gratefully acknowledge the generous help from Flow and Image Cytometry Facility, the
649 Pathology Resource Network, Preclinical Imaging Services, Experimental Tumor Model Shared
650 Resource, and Laboratory Animal Resource (LAR), Ninfa L. Straubinger for technical assistance
651 with the PDAC models. We thank Drs. Bert Vogelstein and Alessandro Carugo for their
652 generous gifts of cell lines, Drs. Dean Tang and David Goodrich for discussion of the
653 manuscript. This work supported by NIH R21CA259719 and DoD BC220542 (to AVB), NIH
654 R37CA282430 (to CF and AVB), Roswell Park Alliance Foundation (to AVB and CF), NIH

655 R01CA198096 to R.M.S., NIH grant AI164081 (to TM), in part by NIH R25CA181003, the
656 Deanship of Scientific Research at Northern Border University, Arar, KSA the project number
657 "NBU-SAFIR-2024 to (MMA), and the Roswell Park Comprehensive Cancer Center Support
658 Grant, P30CA016056. Research reported in this publication was supported by the National
659 Institutes of Health Office of Research Infrastructure Programs under award number
660 S10OD024973 [49]. The content is solely the responsibility of the authors and does not necessarily
661 represent the official views of the National Institutes of Health. Computational support was
662 provided by the Center for Computational Research at the University at Buffalo [50].

663 **ETHICS STATEMENT**

664 The study protocol was approved by the Institute Animal Care and Use Committee (IACUC).
665 The facility is certified by the American Association for Accreditation of Laboratory Animal
666 Care (AAALAC) and in accordance with current regulation and standards of the US Department
667 of Agriculture and the US Department of Health and Human Services.

668

669 **MATERIALS AVAILABILITY**

670 Patient-derived xenograft colorectal cancer models are available from the lead contact (A.B.)
671 under a Material Transfer Agreement.

672 **LEAD CONTACT**

673 Further information and requests for resources and reagents should be directed to and will be
674 fulfilled by the lead contact, prof. Andrei Bakin (Andrei.Bakin@roswellpark.org)

675

676 **FIGURE LEGENDS**

677 **Figure 1. The combination of TAS102 and talazoparib induces DNA damage response and**
678 **the G2 checkpoint.** (**a-b**) Cell-cycle analysis of HCT116 p53WT and p53KO, and DLD1
679 ($p53^{S241F}$) cell lines treated with vehicle control (C), 100nM talazoparib (Tal), 500 nM TAS102
680 (TAS) or their combination (TAS+Tal) for 24 hours. Cells were stained with Hoechst for DNA
681 content and analyzed by flow cytometry. (**b**) Quantification of cell cycle data. Comparisons were
682 made using two-way ANOVA (∗p < 0.05, ∗∗p < 0.01, ∗∗∗p < 0.001, ∗∗∗∗p < 0.0001).
683 Experiments were repeated at least two times. (**c-d**) Immunoblots of whole-cell extracts from cell
684 lines treated with vehicle control (C), 100 nM talazoparib (T), 500 nM TAS102 (TAS), their
685 combination (TT), or 50 nM nocodazole (Nc) for 24 hours. (**e-f**) Quantification of phospho-
686 CDK1 and phospho-H3 levels in CRC PDX-02-07-RP ($p53^{H179R}$) tissues (**e**), and PDX-01-03-RP
687 (p53WT) tissues (**f**). PDX tumor bearing mice were treated by oral gavage with vehicle-control,
688 talazoparib, TAS102, or TAS102-talazoparib. Comparisons were done using one-way ANOVA
689 (*p < 0.05, **p < 0.01, ***p < 0.001, and ****p < 0.0001). (**g**) Working model.

690

691 **Figure 2. Transcriptomic changes in p53WT and p53KO cells following TAS102 and**
692 **talazoparib treatment.** Volcano plots show differential gene expression between control and
693 treatment groups (talazoparib, TAS102, and combination) for both HCT116 p53WT (**a-c**) and
694 p53KO (**d-f**) cell lines. Red data points represent genes that meet both the adjusted p-value <0.05

695 and a pre-defined log2 fold change (FC) threshold. Blue data points indicate genes that only meet
696 the log2 FC threshold, gray dots show non-significant genes. (**g-h**) Venn diagrams show the
697 overlap of differentially expressed genes among the treatment groups in HCT116 p53WT (**g**) and
698 p53KO (**h**) cells. (**i**) Heatmaps show the expression profiles of select genes across the control and
699 treatment groups in HCT116 p53WT (left) and p53KO (right) cells. Gene lists are curated from
700 KEGG and Cyclebase_3.0 databases.
701
702 **Figure 3. G2 checkpoint kinase inhibitors enhance the cytotoxic effects of TAS102 and**
703 **talazoparib treatment.** (**a-d**) Dose-response curves for a panel of colorectal cancer cell lines
704 treated with increasing concentrations of TAS102 in the presence of 100 nM talazoparib. Cells
705 were co-treated for 72 hours with varying concentrations of the ATR inhibitor AZD6738
706 (ATRi; 50nM, 100nM, 250nM, and 500nM). (**e-i**) Cells were treated as described above with the
707 CHK1 inhibitor, AZD7762 (CHK1i; 50, 100, 250, and 500 nM). (**j-m**) Cells were treated as
708 described above with the WEE1 inhibitor, MK-1775 (WEE1i; 50, 100, 250, and 500 nM). All
709 data were normalized to untreated control. The half-maximal inhibitory concentration (IC50)
710 values were determined using three-parameter nonlinear regression. All experiments were
711 performed with at least two biological replicates and six technical replicates. (**n-o**) Cytotoxicity
712 parameters in p53WT and mutant cell lines. Combination Index (CI) values were calculated for
713 combinations with ATRi (**n**) and WEE1i (**o**) across several concentrations.
714
715 **Figure 4. Combination treatment with TAS102 and talazoparib induces a prolonged G2**
716 **arrest in p53-mutant cancer cells.** (**a-c**) Cell cycle analysis was performed on cell lines treated
717 with vehicle control (C), 500nM TAS102 and 100nM talazoparib for 24 hours (**T0**) followed by
718 incubation in drug-free medium. All experiments were done in at least two independent
719 biological replicates. (**d-g**) Immunoblotting on whole-cell extracts from HCT116-p53WT,
720 HCT116-p53KO, HCT116-p53$^{R248W/-}$ and HT29 cell lines treated as described above (**a-c**). The
721 experiments were repeated in at least two independent biological replicates and two technical
722 replicates. Blots were probed with antibodies to phopsho-CHK1, p53, cyclin D1, phospho-
723 CDK1, p21, phospho-H2AX (γH2AX), phospho-histone H3, and GAPDH as a loading control.
724
725 **Figure 5. The dynamics of DNA damage repair in response to combined TAS102 and**
726 **talazoparib treatment.** (**a**) Immunofluorescence microscopy images of p53WT cells stained for
727 γH2AX (green), a DNA damage marker, and RAD51 (red), a homologous recombination
728 component, along with Hoechst 33342 (blue; nucleus). Cells were treated with vehicle-control
729 (CTR) or 500nM TAS102 plus 100nM talazoparib (**T0**) for 24 hours, followed by drug
730 withdrawal and the cells were allowed to recover. All images were taken using 100x lens; scale
731 bar 10μm. (**b, h**) Enlarged images of regions highlighted in the main panels show the co-
732 localization of γH2AX and RAD51 foci at T0 in MCF10A cells and at 24 hours in DLD1 cells.
733 Arrows indicate the positions of these foci. (**c**) Enlarged images of Hoechst-stained cells at CTR,
734 T0, and 72hours. (**d-e, j-k, m-n**) Quantitative analysis of corrected total cellular fluorescence
735 (CTCF) for γH2AX (**d, j, m**) and RAD51 (**e, k, n**) was performed on a minimum 40 cells per
736 treatment group. The graphs show representative median scattered dot plots. Comparisons were
737 made using the two-way ANOVA (****, $P<0.001$). (**f, l, o**) The nuclear area was measured from
738 Hoechst-stained cells, with at least 40 cells/group. All experiments were done at least two times.
739

740 **Figure 6. Sequential application of WEE1 inhibitor enhances the cytotoxicity of TAS102-**
741 **talazoparib treatment in p53-deficient cancer cells.** (**a-e**) Cytotoxicity curves for p53 wild-
742 type (MCF10A and HCT116), and p53-deficient (HCT116-p53KO, HCT116-p53$^{R248W/-}$, HT29)
743 cells. Cells were treated with increasing concentrations of TAS102 plus 100nM talazoparib for
744 24 hours. After a 24-hour drug washout, cells were incubated with 50, 100, 250, or 500 nM of
745 the WEE1 inhibitor (WEE1i) for an additional 72 hours. (**f**) Combination index (CI) analysis for
746 the tested WEE1i concentrations. Data are presented as mean ± SEM from at least two
747 independent biological replicates, each with six technical replicates. (**g**) Flow cytometry analysis
748 of cells treated with vehicle control or a sequential regimen of 500 nM TAS102 plus 100 nM
749 talazoparib, followed by 250 nM WEE1i. Cells were stained with propidum iodide and annexin-
750 V. (**h-k**) Quantification of Annexin V and propidium iodide (PI) double-positive cells from two
751 biological replicates. Statistical significance was determined using one-way ANOVA (*$p < 0.05$,
752 **$p < 0.01$, ***$p < 0.001$, and ****$p < 0.0001$).
753
754 **Figure 7. A sequential application of WEE1 inhibitor enhances the efficacy of TAS102-**
755 **talazoparib treatment in p53 mutant cancer models.** (**a-d**) SCID mice (10mice/group) were
756 subcutaneously implanted with colon cancer HT29 cells. At tumor size of 100mm^3, mice were
757 randomized into four treatment groups: vehicle control, WEE1 inhibitor (WEE1i, MK1775, 60
758 mg/kg), a combination of TAS102 (50 mg/kg) and talazoparib (0.15 mg/kg), and a sequential
759 regimen consisting of one week of TAS102/talazoparib followed by one week of the WEE1
760 inhibitor. All treatments were administered *via* oral gavage on a schedule of five days ON and
761 two days OFF. Tumor growth was measured twice weekly, and statistical significance was
762 determined using a two-way ANOVA (*$p < 0.05$). (**b**) Tumor growth inhibition (TGI) was
763 calculated as TGI = 100% x [Vehicle − Treatment) / Vehicle]. Comparisons were made using a
764 one-way ANOVA (**, $P<0.01$, ***, $P<0.001$, ****, $P<0.001$). (**c**) Survival was evaluated using
765 Kaplan-Meier estimator based on time-to-arrive at 750 mm^3 of tumor size. The comparison was
766 made using the log-rank test. (**d**) Mouse body weights were measured twice per week over the
767 course of study. (**e-h**) Patient-derived tumor xenografts (PDXs) from a patient with PDAC
768 (PDAC-14312-4p) were subcutaneously implanted into SCID mice (10 mice/group). At 100
769 mm^3, mice were randomized and treated as described above for HT29 xenografts. (**f**) Tumor
770 growth inhibition in the PDX model was calculated as described in (**b**). Comparisons were made
771 using a one-way ANOVA (**, $P<0.01$, ***, $P<0.001$, ****, $P<0.001$). (**g**) Survival was evaluated
772 using Kaplan-Meier estimator based on time to arrive at 750 mm3 of tumor size. Group
773 comparisons were performed with the log-rank test. (**h**) Mouse body weights were measured
774 twice weekly over the course of study. (**i-l**) Patient-derived tumor xenografts (PDXs) from a
775 colorectal cancer patient (PDX-3B1-29-RP-3p) were subcutaneously implanted into SCID mice
776 (10 mice/group). Experiments and the analysis were done essentially as described for (**e-h**). (**m**)
777 A model of the triple-drug drug strategy acting as an *inducer-amplifier-terminator* trio in p53
778 mutant cancers.
779
780
781

782 **REFERENCES**

783 1. Siegel RL, Giaquinto AN, Jemal A. Cancer statistics, 2024. CA Cancer J Clin.
784 2024;74(1):12-49.
785 2. Ladabaum U, Dominitz JA, Kahi C, Schoen RE. Strategies for Colorectal Cancer Screening.
786 Gastroenterology. 2020;158(2):418-32.
787 3. Patel SG, Karlitz JJ, Yen T, Lieu CH, Boland CR. The rising tide of early-onset colorectal
788 cancer: a comprehensive review of epidemiology, clinical features, biology, risk factors,
789 prevention, and early detection. Lancet Gastroenterol Hepatol. 2022;7(3):262-74.
790 4. Siegel RL, Wagle NS, Cercek A, Smith RA, Jemal A. Colorectal cancer statistics, 2023. CA
791 Cancer J Clin. 2023;73(3):233-54.
792 5. Biller LH, Schrag D. Diagnosis and Treatment of Metastatic Colorectal Cancer: A Review.
793 Jama. 2021;325(7):669-85.
794 6. Wolfgang CL, Herman JM, Laheru DA, Klein AP, Erdek MA, Fishman EK, et al. Recent
795 progress in pancreatic cancer. CA Cancer J Clin. 2013;63(5):318-48.
796 7. Neoptolemos JP, Kleeff J, Michl P, Costello E, Greenhalf W, Palmer DH. Therapeutic
797 developments in pancreatic cancer: current and future perspectives. Nature reviews
798 Gastroenterology & hepatology. 2018;15(6):333-48.
799 8. Nakayama M, Oshima M. Mutant p53 in colon cancer. J Mol Cell Biol. 2019;11(4):267-76.
800 9. Muller PAJ, Vousden KH. Mutant p53 in cancer: new functions and therapeutic
801 opportunities. Cancer Cell. 2014;25(3):304-17.
802 10. Sabapathy K, Lane DP. Therapeutic targeting of p53: all mutants are equal, but some mutants
803 are more equal than others. Nature reviews Clinical oncology. 2018;15(1):13-30.
804 11. Wang H, Guo M, Wei H, Chen Y. Targeting p53 pathways: mechanisms, structures, and
805 advances in therapy. Signal Transduct Target Ther. 2023;8(1):92.
806 12. Reinhardt HC, Aslanian AS, Lees JA, Yaffe MB. p53-deficient cells rely on ATM- and
807 ATR-mediated checkpoint signaling through the p38MAPK/MK2 pathway for survival after
808 DNA damage. Cancer Cell. 2007;11(2):175-89.
809 13. Mendez E, Rodriguez CP, Kao MC, Raju S, Diab A, Harbison RA, et al. A Phase I Clinical
810 Trial of AZD1775 in Combination with Neoadjuvant Weekly Docetaxel and Cisplatin before
811 Definitive Therapy in Head and Neck Squamous Cell Carcinoma. Clin Cancer Res.
812 2018;24(12):2740-8.
813 14. Leijen S, Beijnen JH, Schellens JH. Abrogation of the G2 checkpoint by inhibition of Wee-1
814 kinase results in sensitization of p53-deficient tumor cells to DNA-damaging agents. Current
815 clinical pharmacology. 2010;5(3):186-91.
816 15. Durinikova E, Reilly NM, Buzo K, Mariella E, Chilà R, Lorenzato A, et al. Targeting the
817 DNA Damage Response Pathways and Replication Stress in Colorectal Cancer. Clinical cancer
818 research : an official journal of the American Association for Cancer Research.
819 2022;28(17):3874-89.
820 16. Lheureux S, Cristea MC, Bruce JP, Garg S, Cabanero M, Mantia-Smaldone G, et al.
821 Adavosertib plus gemcitabine for platinum-resistant or platinum-refractory recurrent ovarian
822 cancer: a double-blind, randomised, placebo-controlled, phase 2 trial. Lancet.
823 2021;397(10271):281-92.
824 17. Zonneville J, Wang M, Alruwaili MM, Smith B, Melnick M, Eng KH, et al. Selective
825 therapeutic strategy for p53-deficient cancer by targeting dysregulation in DNA repair.
826 Communications biology. 2021;4(1):862.

827 18. Alruwaili MM, Zonneville J, Naranjo MN, Serio H, Melendy T, Straubinger RM, et al. A
828 synergistic two-drug therapy specifically targets a DNA repair dysregulation that occurs in p53-
829 deficient colorectal and pancreatic cancers. Cell Rep Med. 2024;5(3):101434.
830 19. Fountzilas C, Witkiewicz A, Chatley S, Fitzpatrick V, Zonneville J, Alruwaili M, et al.
831 YIA24-003: A Phase I Study of TAS102 Plus Talazoparib in Advanced Colorectal (CRC) and
832 Esophagogastric (EGC) Adenocarcinomas. Journal of the National Comprehensive Cancer
833 Network. 2024;22(2.5):YIA24-003.
834 20. Voit R, Seiler J, Grummt I. Cooperative Action of Cdk1/cyclin B and SIRT1 Is Required for
835 Mitotic Repression of rRNA Synthesis. PLoS genetics. 2015;11(5):e1005246.
836 21. Smith J, Tho LM, Xu N, Gillespie DA. The ATM-Chk2 and ATR-Chk1 pathways in DNA
837 damage signaling and cancer. Advances in cancer research. 2010;108:73-112.
838 22. Castedo M, Perfettini JL, Roumier T, Andreau K, Medema R, Kroemer G. Cell death by
839 mitotic catastrophe: a molecular definition. Oncogene. 2004;23(16):2825-37.
840 23. Xie G, Habbersett RC, Jia Y, Peterson SR, Lehnert BE, Bradbury EM, et al. Requirements
841 for p53 and the ATM gene product in the regulation of G1/S and S phase checkpoints.
842 Oncogene. 1998;16(6):721-36.
843 24. Toledo LI, Murga M, Fernandez-Capetillo O. Targeting ATR and Chk1 kinases for cancer
844 treatment: a new model for new (and old) drugs. Mol Oncol. 2011;5(4):368-73.
845 25. Lobrich M, Jeggo PA. The impact of a negligent G2/M checkpoint on genomic instability
846 and cancer induction. Nat Rev Cancer. 2007;7(11):861-9.
847 26. Peng C-Y, Graves PR, Thoma RS, Wu Z, Shaw AS, Piwnica-Worms H. Mitotic and
848 G₂ Checkpoint Control: Regulation of 14-3-3 Protein Binding by Phosphorylation
849 of Cdc25C on Serine-216. Science. 1997;277(5331):1501-5.
850 27. Sanchez Y, Wong C, Thoma RS, Richman R, Wu Z, Piwnica-Worms H, et al. Conservation
851 of the Chk1 Checkpoint Pathway in Mammals: Linkage of DNA Damage to Cdk Regulation
852 Through Cdc25. Science. 1997;277(5331):1497-501.
853 28. Solomon MJ, Lee T, Kirschner MW. Role of phosphorylation in p34cdc2 activation:
854 identification of an activating kinase. Mol Biol Cell. 1992;3(1):13-27.
855 29. Krek W, Nigg EA. Mutations of p34cdc2 phosphorylation sites induce premature mitotic
856 events in HeLa cells: evidence for a double block to p34cdc2 kinase activation in vertebrates.
857 EMBO J. 1991;10(11):3331-41.
858 30. Lee TH, Kirschner MW. An inhibitor of p34cdc2/cyclin B that regulates the G2/M transition
859 in Xenopus extracts. Proc Natl Acad Sci U S A. 1996;93(1):352-6.
860 31. Sausville E, Lorusso P, Carducci M, Carter J, Quinn MF, Malburg L, et al. Phase I dose-
861 escalation study of AZD7762, a checkpoint kinase inhibitor, in combination with gemcitabine in
862 US patients with advanced solid tumors. Cancer Chemother Pharmacol. 2014;73(3):539-49.
863 32. Seto T, Esaki T, Hirai F, Arita S, Nosaki K, Makiyama A, et al. Phase I, dose-escalation
864 study of AZD7762 alone and in combination with gemcitabine in Japanese patients with
865 advanced solid tumours. Cancer Chemother Pharmacol. 2013;72(3):619-27.
866 33. Foote KM, Nissink JWM, McGuire T, Turner P, Guichard S, Yates JWT, et al. Discovery
867 and Characterization of AZD6738, a Potent Inhibitor of Ataxia Telangiectasia Mutated and Rad3
868 Related (ATR) Kinase with Application as an Anticancer Agent. J Med Chem.
869 2018;61(22):9889-907.
870 34. Leijen S, van Geel RM, Pavlick AC, Tibes R, Rosen L, Razak AR, et al. Phase I Study
871 Evaluating WEE1 Inhibitor AZD1775 As Monotherapy and in Combination With Gemcitabine,

872 Cisplatin, or Carboplatin in Patients With Advanced Solid Tumors. J Clin Oncol.
873 2016;34(36):4371-80.
874 35. Chou TC, Talalay P. Quantitative analysis of dose-effect relationships: the combined effects
875 of multiple drugs or enzyme inhibitors. Adv Enzyme Regul. 1984;22:27-55.
876 36. Foucquier J, Guedj M. Analysis of drug combinations: current methodological landscape.
877 Pharmacol Res Perspect. 2015;3(3):e00149.
878 37. Fountzilas C, Witkiewicz A, Chatley S, Fitzpatrick V, Zonneville J, Alruwaili M, et al. A
879 Phase I Study of TAS102 Plus Talazoparib in Advanced Colorectal (CRC) and Esophagogastric
880 (EGC) Adenocarcinomas. Journal of the National Comprehensive Cancer Network.
881 2024;22(2.5):YIA24-003.
882 38. Shirole NH, Pal D, Kastenhuber ER, Senturk S, Boroda J, Pisterzi P, et al. TP53 exon-6
883 truncating mutations produce separation of function isoforms with pro-tumorigenic functions.
884 eLife. 2016;5:e17929.
885 39. Barr PJ, Nolan PA, Santi DV, Robins MJ. Inhibition of thymidylate synthetase by 5-alkynyl-
886 2'-deoxyuridylates. Journal of medicinal chemistry. 1981;24(12):1385-8.
887 40. Pettersen HS, Visnes T, Vagbo CB, Svaasand EK, Doseth B, Slupphaug G, et al. UNG-
888 initiated base excision repair is the major repair route for 5-fluorouracil in DNA, but 5-
889 fluorouracil cytotoxicity depends mainly on RNA incorporation. Nucleic Acids Res.
890 2011;39(19):8430-44.
891 41. Murai J, Huang SY, Das BB, Renaud A, Zhang Y, Doroshow JH, et al. Trapping of PARP1
892 and PARP2 by Clinical PARP Inhibitors. Cancer Res. 2012;72(21):5588-99.
893 42. Shiloh Y, Ziv Y. The ATM protein kinase: regulating the cellular response to genotoxic
894 stress, and more. Nat Rev Mol Cell Biol. 2013;14(4):197-210.
895 43. Lavin MF. ATM and the Mre11 complex combine to recognize and signal DNA double-
896 strand breaks. Oncogene. 2007;26(56):7749-58.
897 44. Zhang X, Li J, Sejas DP, Pang Q. The ATM/p53/p21 pathway influences cell fate decision
898 between apoptosis and senescence in reoxygenated hematopoietic progenitor cells. J Biol Chem.
899 2005;280(20):19635-40.
900 45. Saldivar JC, Hamperl S, Bocek MJ, Chung M, Bass TE, Cisneros-Soberanis F, et al. An
901 intrinsic S/G(2) checkpoint enforced by ATR. Science. 2018;361(6404):806-10.
902 46. Foo TK, Vincelli G, Huselid E, Her J, Zheng H, Simhadri S, et al. ATR/ATM-Mediated
903 Phosphorylation of BRCA1 T1394 Promotes Homologous Recombinational Repair and G(2)-M
904 Checkpoint Maintenance. Cancer Res. 2021;81(18):4676-84.
905 47. Rogakou EP, Pilch DR, Orr AH, Ivanova VS, Bonner WM. DNA double-stranded breaks
906 induce histone H2AX phosphorylation on serine 139. J Biol Chem. 1998;273(10):5858-68.
907 48. Britton S, Chanut P, Delteil C, Barboule N, Frit P, Calsou P. ATM antagonizes NHEJ
908 proteins assembly and DNA-ends synapsis at single-ended DNA double strand breaks. Nucleic
909 Acids Res. 2020;48(17):9710-23.
910 49. Furlani T, Matott L. Acquisition of High-Performance Data and Computing Infrastructure to
911 Advance Biomedical Research2019.
912 50. UBCCR. Center for Computational Research, University at Buffalo. 2021. CCR Facility
913 Description.
914

915

916 **KEY RESOURCES TABLE**

REAGENT or RESOURCE	SOURCE	IDENTIFIER
Antibodies		
anti-p53 (Mouse Monoclonal antibody, Clone do-1)	Santa Cruz Biotechnology	Cat# sc-126; RRID:AB_628082
anti-p21 (CDKN1A), F-5 mouse monoclonal	Santa Cruz Biotechnology	Cat# sc-6246; RRID:AB_628073
anti-phospho-Ser15 p53 (rabbit, polyclonal)	Cell Signaling Technology	Cat# 9284; RRID:AB_331464
anti-PARP1 (mouse monoclonal antibody, Clone 5a5)	Santa Cruz Biotechnology	Cat# sc-56197; RRID:AB_630080
anti-phospho-Ser139 H2AX (γH2AX; rabbit polyclonal)	Abcam	Cat# ab-11174; RRID:AB_297813
anti-Thymidylate Synthase (TS106)	Millipore	Cat# MAB4130, RRID:AB_2210729
anti-phospho-Tyr15-CdC2	Santa Cruz	Cat# sc-136014, RRID:AB_2016914
anti-phospho-Chk1 (Ser325)	Cell signaling	Cat# 2348, RRID:AB_331212
anti-phospho HH3 (Ser10)	Cell signaling	Cat# 31261, RRID:AB_3076725
anti-Cyclin A2	Invitrogen	Cat# MA1-180, RRID:AB_2633305
anti-bromodeoxyuridine, anti-BrdU	Dako	Cat# M0744, RRID:AB_10013660
anti-cleaved Caspase-3 (Asp175)	Cell signaling	Cat# 9661, RRID:AB_2341188
Rabbit anti-gamma-H2AX (phospho-Ser139) Antibody	Bethyl	Cat# A300-081A, RRID:AB_203288
anti-Human Ki67/MKI67 Antibody	R&D Systems	Cat#: IC7617S, RRID:AB_2889352
anti-Rad51 antibody	Abcam	Cat# ab133534, RRID:AB_2722613
anti-phospho-Ser139 H2AX (γH2AX; mouse mAb, JBW301)	Millipore	Cat# 05-636; RRID:AB_309864
anti-BrdU antibody (3D4), FITC conjugate	Biolegend	Cat#364104; RRID:AB_2564481
Goat Anti-Rabbit IgG (H L)-HRP Conjugate antibody	Bio-Rad	Cat# 170-6515; RRID:AB_11125142
Goat Anti-Mouse IgG (H L)-HRP Conjugate antibody	Bio-Rad	Cat# 170-6516; RRID:AB_11125547
Biological samples: Patient Derived Xenografts (PDXs)		
PDAC PDX-14312-4p	Dr. Robert Straubinger (University at Buffalo)	SUNY at Buffalo
CRC PDX-3B1-29-RP-3p	Dr. Andrei Bakin (Roswell Park)	PDX-3B1-29-RP

Chemicals, peptides, and recombinant proteins		
Talazoparib (Synonyms: BMN-673)	Adooq	Cat# A15533
TAS102 (trifluorthymidine (trifluridine)/tipiracil HCl mix)	Adooq	Cat# A11243
5-ethynyl-2'-deoxyuridine (EdUrd)	Lumiprobe	Cat# 20540
Cy3-azide	Lumiprobe	Cat#B1030
CellTrace Violet Dye	Invitrogen	Cat#C34557
AFDye 488 Azide	Click Chemistry Tools, Scottsdale, AZ	Cat#1275-1
THPTA (tris-hydroxypropyltriazolylmethylamine)	Click Chemistry Tools, Scottsdale, AZ	Cat#1010-500
RNase A (10 mg/mL)	Thermo Fisher Scientific	Cat#EN0531
D-luciferin	Gold Biotechnology, St Louis	LUCK-1G
Copper sulfate, Cu(II)SO4	Sigma-Aldrich	Cat# 61230
Hydroxyurea	Sigma-Aldrich	Cat#55291
(2-Hydroxypropyl)-β-cyclodextrin (HPCD; Cavasol)	Sigma-Aldrich	Cat#778907
Bovine serum albumin (BSA)	Sigma-Aldrich	Cat#A2153
Dimethyl sulfoxide (DMSO)	Sigma-Aldrich	Cat#D8418
Boric acid	Sigma-Aldrich	Cat#B6768
Propidium iodide	Sigma-Aldrich	Cat#P4170
Hoechst 33342	Sigma-Aldrich	Cat#B2261
Methylene Blue hydrate	Sigma-Aldrich	Cat#M9140-100G
Paraformaldehyde	Sigma-Aldrich	Cat#158127
Dialyzed FBS (fetal bovine serum)	Gibco	Cat#A33820
ECL Western Blotting Substrate, Pierce	Thermo Fisher Scientific	Cat# 32106
SuperSignal™ West Atto Ultimate Sensitivity Substrate	Thermo Fisher Scientific	Cat#A38555
SDS (Sodium Dodecyl Sulfate)	Bio-Rad	Cat#1610301
DC™ Protein Assay Kit I	Bio-Rad	Cat#5000111
Tween 20, 100% Nonionic Detergent	Bio-Rad	Cat#1706531
Matrigel Matrix GFR	VWR International	Cat# 47743-720
Critical commercial assays		
Caspase-Glo® 3/7 Assay System	Promega	Cat#G8090
Deposited data		
Gene Expression and Mutation Counts	Pan-CANCER-TCGA	Cbioportal.org
Experimental models: Cell lines		
HCT-116 (p53-WT)	Dr. Bert Vogelstein (Johns Hopkins)	RRID:CVCL_0291
HCT-116-p53-KO; HCT-116 TP53(-/-); HCT116-p53-null	Dr. Bert Vogelstein (Johns Hopkins)	RRID:CVCL_HD97

HCT-116-p53-R248W/-	Dr. Bert Vogelstein (Johns Hopkins)	RRID:CVCL_RJ68
RKO	Dr. Alessandro Carugo (IRBM European School of Molecular Medicine, Lazio, Italia)	RRID:CVCL_0504
RKO-p53(-/-); RKO-p53KO; RKO-p53-null	Dr. Alessandro Carugo (IRBM ESMM, Lazio, Italia)	
HT29; HT-29	ATCC	RRID:CVCL_0320
MIAPACA2; MiaPaCa-2	ATCC	RRID:CVCL_0428
MCF10A	ATCC	RRID:CVCL_0598
MDA-MB-231	ATCC	RRID:CVCL_0062
HPNE; hTERT-Human Pancreatic Nestin-Expressing cells	ATCC	RRID:CVCL_C466
DLD1	ATCC	RRID:CVCL_0248
PANC-1	ATCC	RRID:CVCL_0480
Experimental models: Organisms/strains		
Mouse: SCID/CB17, Balb/c background	Roswell Park Colony	
Mouse: NOD.Cg-Prkdcscid Il2rgtm1Wjl/SzJ (NSG) mice, Balb/c background	Jackson Laboratory	
Software and algorithms		
GraphPad PRISM 10.1.2	GraphPad Software	https://www.graphpad.com/
R/RStudio v4.0.4	The R Foundation	https://www.r-project.org/
FCS Express 7 (Version 7.04.0016)	De Novo software	FCS Express Flow Cytometry Software - De Novo Software
Image J	NIH	https://imagej.net/software/imagej/
HeskaView Integrated Software (version 2.5.2)	Heska	Element HT5 - Heska
Aperio ImageScope (version 12.4.0.5043)	Leica Biosystems	
MetaVue imaging software (Version 7.7.3)	Molecular Devices	
FACSDiva (Version 6.1.3)	Beckman Coulter	
Other		
Nikon TE2000-E inverted microscope	Nikon, USA	
CoolSNAP HQ (CCD camera)	Photometrics, USA	
LSRFortessa Cytometer	BD Biosciences, USA	
VERITAS microplate luminometer	Promega, USA	
Nanodrop	Thermo Fisher, USA	

917

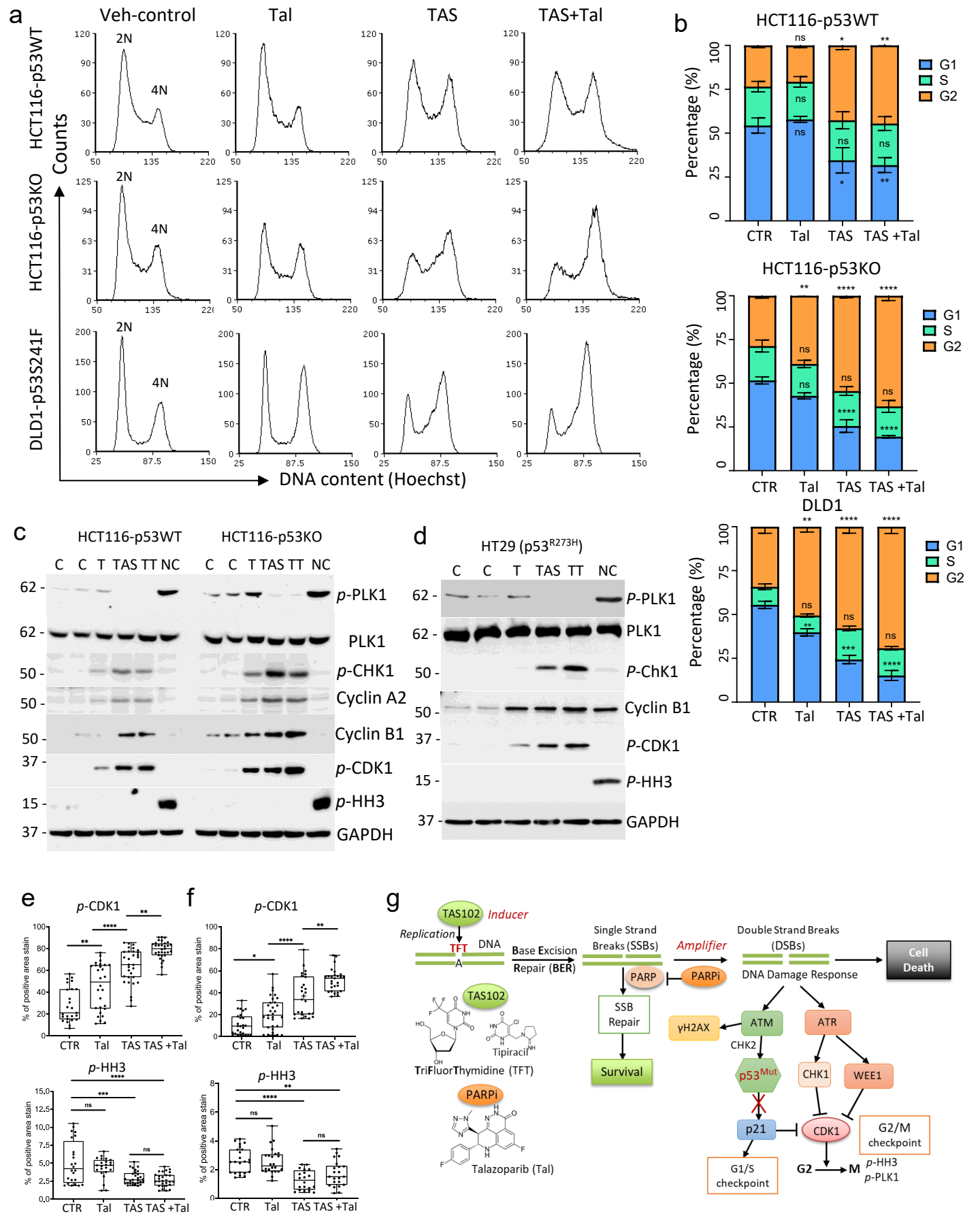
a
Veh-control
Tal
TAS
TAS+Tal
HCT116-p53WT
HCT116-p53KO
DLD1-p53S241F
Counts
2N
4N
DNA content (Hoechst)
b
HCT116-p53WT
HCT116-p53KO
DLD1
Percentage (%)
G1
S
G2
CTR
Tal
TAS
TAS +Tal
c
HCT116-p53WT
HCT116-p53KO
C C T TAS TT NC
p-PLK1
PLK1
p-CHK1
Cyclin A2
Cyclin B1
p-CDK1
p-HH3
GAPDH
d
HT29 (p53R273H)
C C T TAS TT NC
P-PLK1
PLK1
P-ChK1
Cyclin B1
P-CDK1
P-HH3
GAPDH
e
p-CDK1
p-HH3
% of positive area stain
CTR
Tal
TAS
TAS +Tal
f
p-CDK1
p-HH3
% of positive area stain
CTR
Tal
TAS
TAS +Tal
g
TAS102
Inducer
Replication
TFT
DNA
A
Base Excision Repair (BER)
Single Strand Breaks (SSBs)
Amplifier
Double Strand Breaks (DSBs)
Cell Death
PARP
PARPi
DNA Damage Response
SSB Repair
Survival
γH2AX
ATM
ATR
CHK2
p53Mut
CHK1
WEE1
p21
CDK1
G2/M checkpoint
G1/S checkpoint
G2
M
p-HH3
p-PLK1
TAS102
Tipiracil
TriFluorThymidine (TFT)
PARPi
Talazoparib (Tal)

Fig. 2

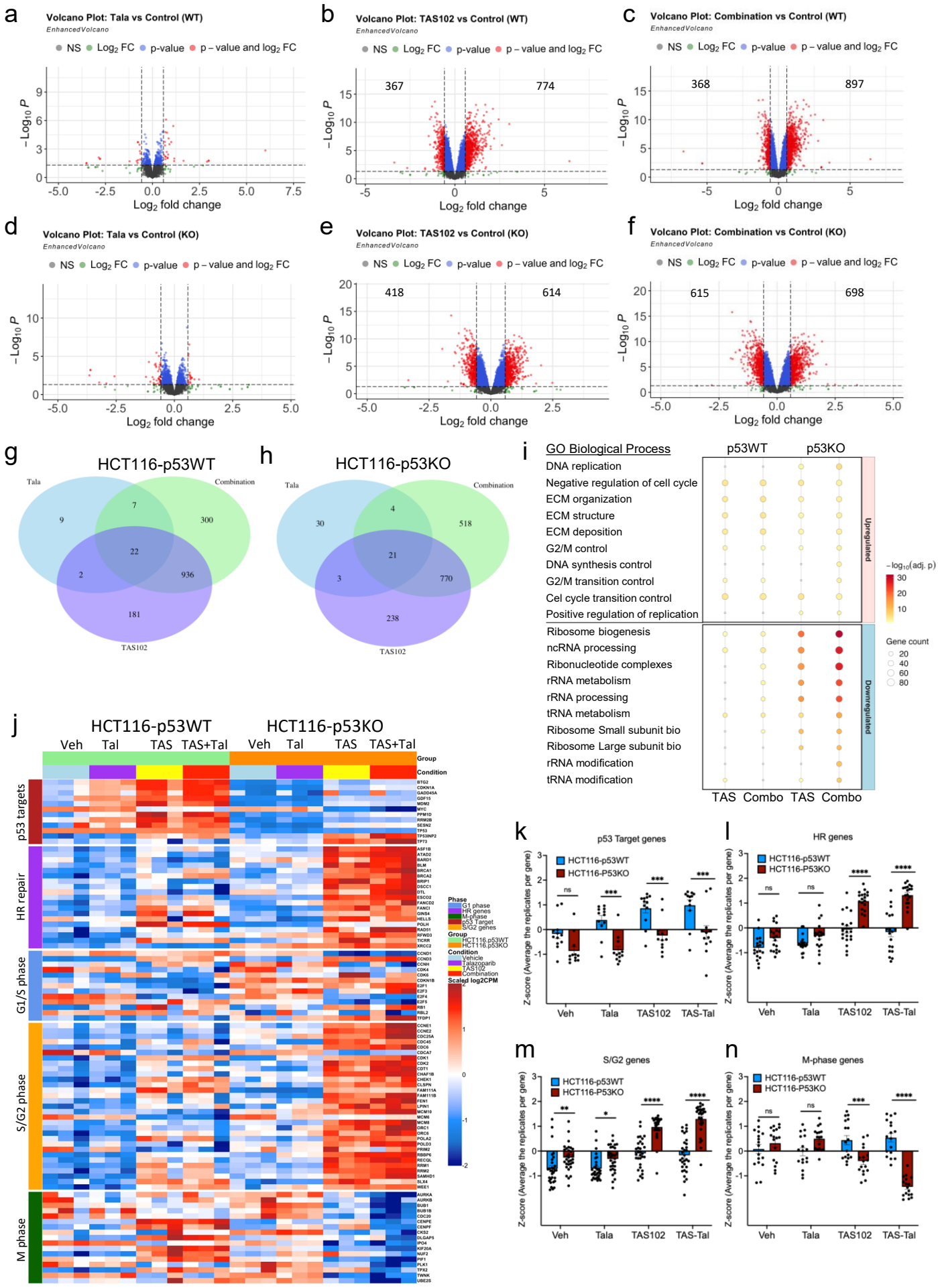
a
Volcano Plot: Tala vs Control (WT)
b
Volcano Plot: TAS102 vs Control (WT)
367
774
c
Volcano Plot: Combination vs Control (WT)
368
897
d
Volcano Plot: Tala vs Control (KO)
e
Volcano Plot: TAS102 vs Control (KO)
418
614
f
Volcano Plot: Combination vs Control (KO)
615
698
NS
Log2 FC
p-value
p – value and log2 FC
Log2 fold change
g
HCT116-p53WT
Tala
Combination
TAS102
h
HCT116-p53KO
i
GO Biological Process
p53WT
p53KO
DNA replication
Negative regulation of cell cycle
ECM organization
ECM structure
ECM deposition
G2/M control
DNA synthesis control
G2/M transition control
Cel cycle transition control
Positive regulation of replication
Ribosome biogenesis
ncRNA processing
Ribonucleotide complexes
rRNA metabolism
rRNA processing
tRNA metabolism
Ribosome Small subunit bio
Ribosome Large subunit bio
rRNA modification
tRNA modification
Upregulated
Downregulated
TAS
Combo
Gene count
j
HCT116-p53WT
HCT116-p53KO
Veh
Tal
TAS
TAS+Tal
Group
Condition
p53 targets
HR repair
G1/S phase
S/G2 phase
M phase
Phase
G1 phase
HR genes
M-phase
p53 Target
S/G2 genes
HCT116-p53WT
HCT116-p53KO
Vehicle
Talazoparib
TAS102
Combination
Scaled log2CPM
k
p53 Target genes
l
HR genes
m
S/G2 genes
n
M-phase genes
HCT116-p53WT
HCT116-P53KO
Z-score (Average the replicates per gene)
Veh
Tala
TAS102
TAS-Tal

Fig. 3

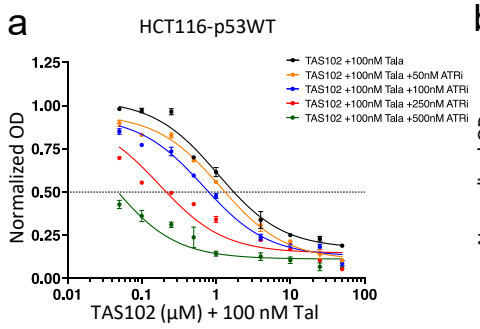

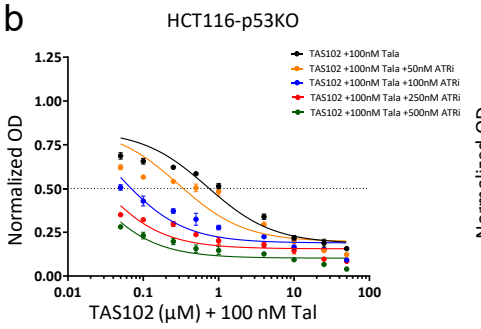

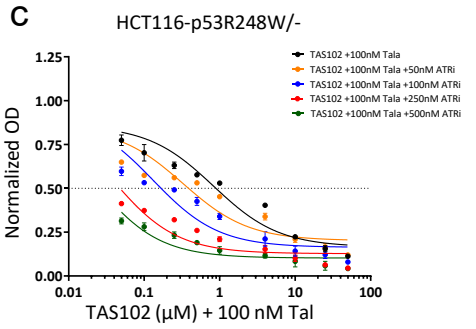

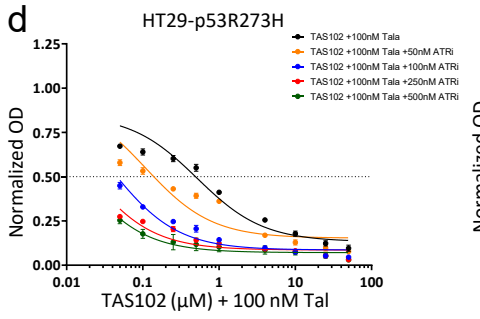

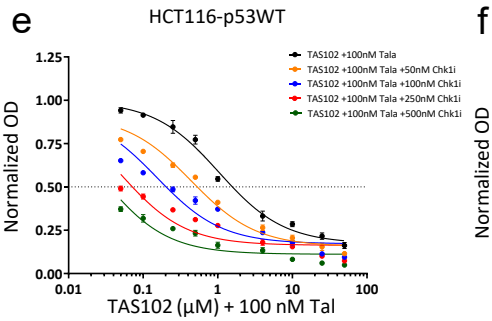

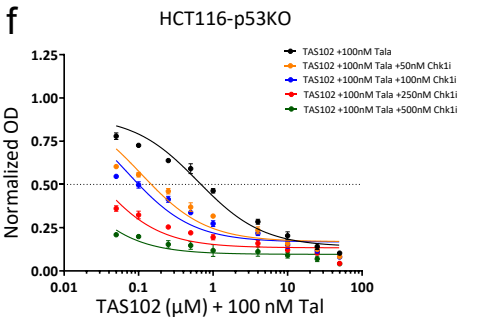

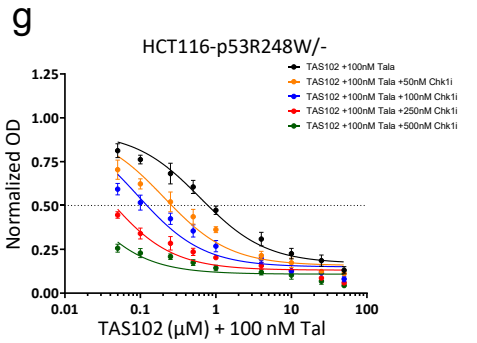

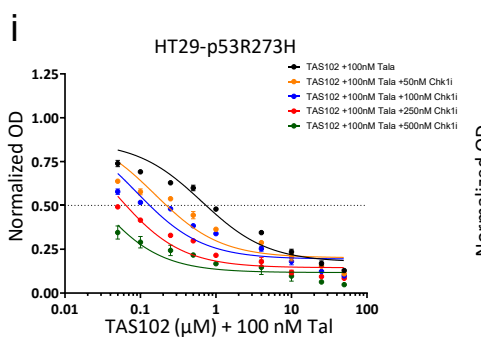

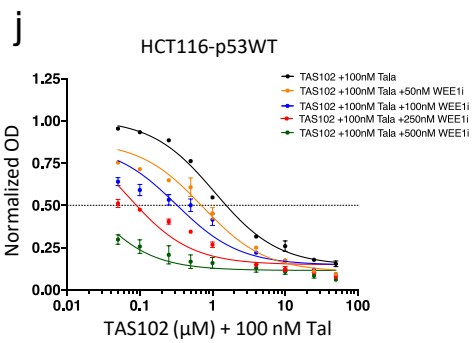

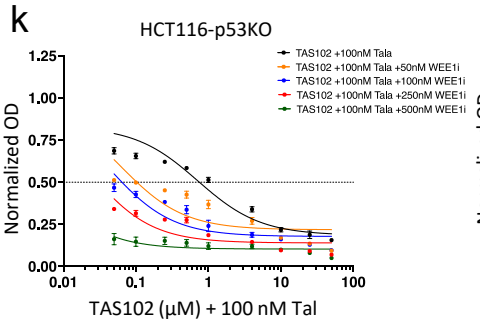

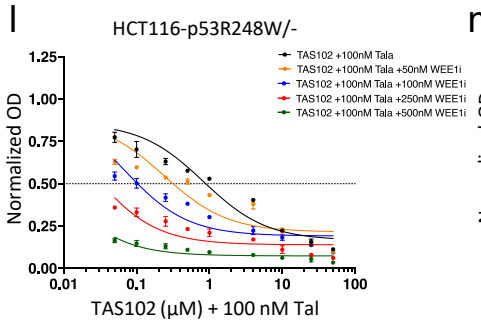

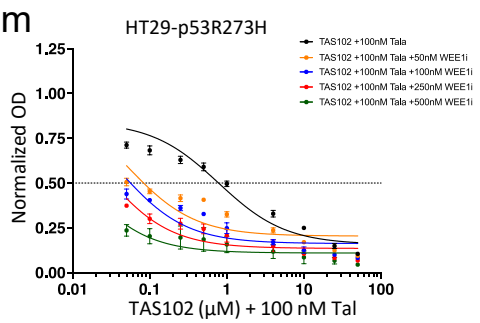

n

			ATR inhibitor		WEE1 inhibitor		CHK1 inhibitor	
Cell line	p53 Status	IC50-TAS102, μM + 100nM Tal	IC50-TAS102, μM + 100nM Tal + 100nM ATRi	Fold change at 100nM ATRi	IC50-TAS102, μM + 100nM Tal + 100nM WEE1i	Fold change at 100nM WEE1i	IC50-TAS102, μM + 100nM Tal + 100nM CHK1i	Fold change at 100nM CHK1i
MCF10A	WT	2.99 ± 0.18	2.94 ± 0.48	1.02	0.99 ± 0.49	2.90	0.13 ± 0.17	2.23
HCT116	WT	1.02 ± 0.06	0.70 ± 0.08	1.45	0.24 ± 0.15	4.64	0.15 ± 0.01	6.93
HCT116	KO	0.77 ± 0.09	0.09 ± 0.06	11.00	0.05 ± 0.01	14.09	0.11 ± 0.05	6.78
HCT116	R248W/-	0.79 ± 0.05	0.19 ± 0.08	4.16	0.10 ± 0.01	7.97	0.28 ± 0.27	3.00
HT29	R273H	0.68 ± 0.23	0.06 ± 0.04	11.33	0.08 ± 0.05	9.09	0.12 ± 0.04	5.82

o

Cell line	p53 Status	CI index ATRi	CI index WEE1i
MCF10A	WT	0.73	0.69
HCT116	WT	0.49	0.42
HCT116	KO	0.21	0.19
HCT116	R248W/-	0.24	0.30
HT29	R273H	0.30	0.16

Fig. 4

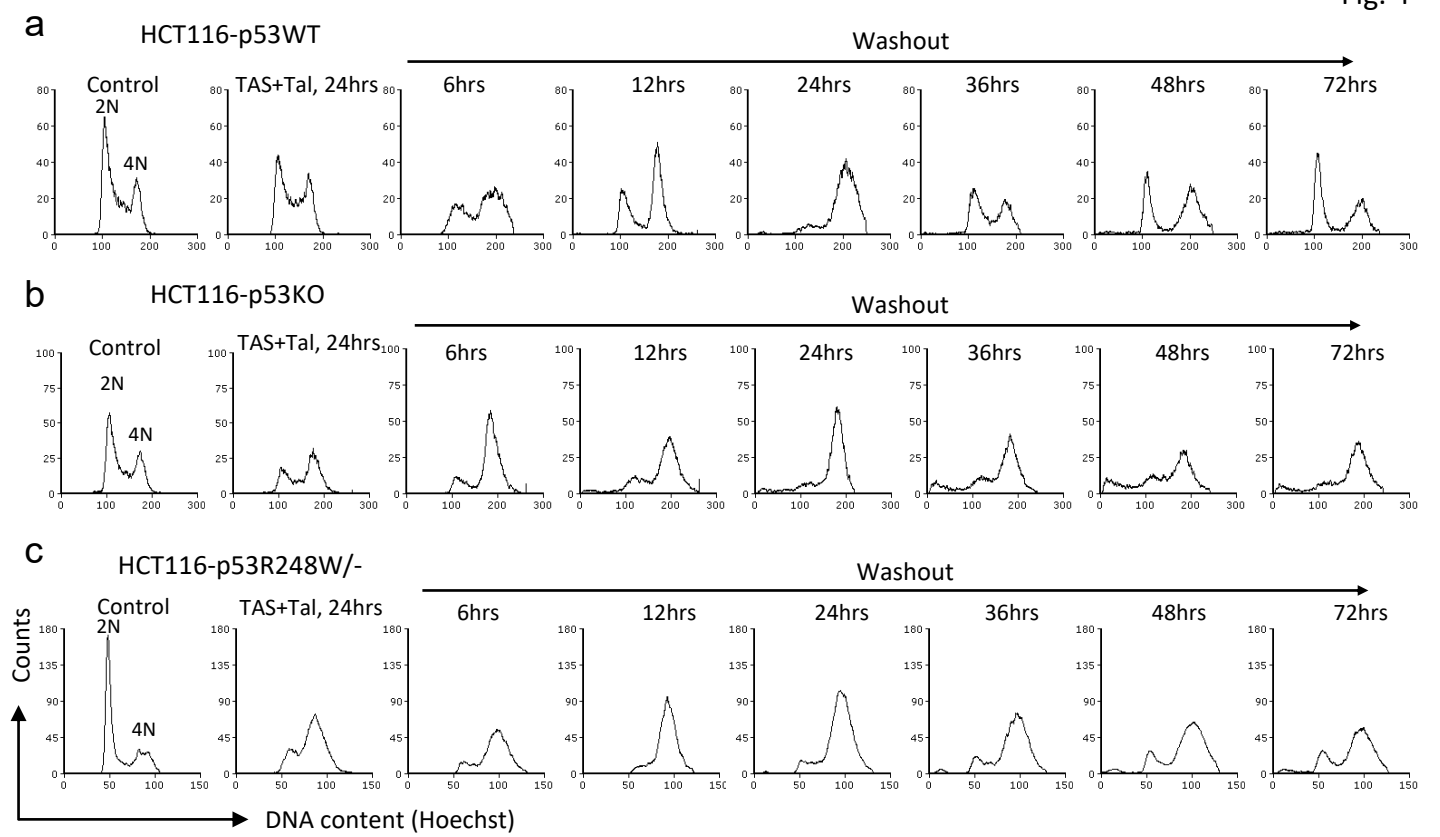
a
HCT116-p53WT
Washout
Control
TAS+Tal, 24hrs
6hrs
12hrs
24hrs
36hrs
48hrs
72hrs
2N
4N
b
HCT116-p53KO
c
HCT116-p53R248W/-
Counts
DNA content (Hoechst)

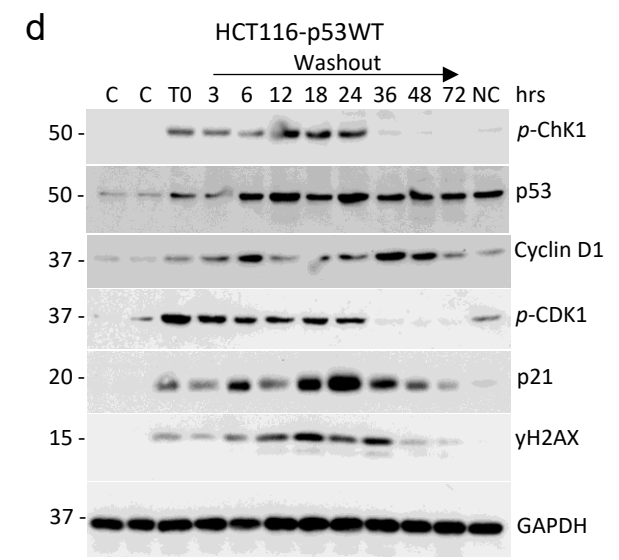
d
HCT116-p53WT
Washout
C C T0 3 6 12 18 24 36 48 72 NC hrs
p-ChK1
p53
Cyclin D1
p-CDK1
p21
γH2AX
GAPDH

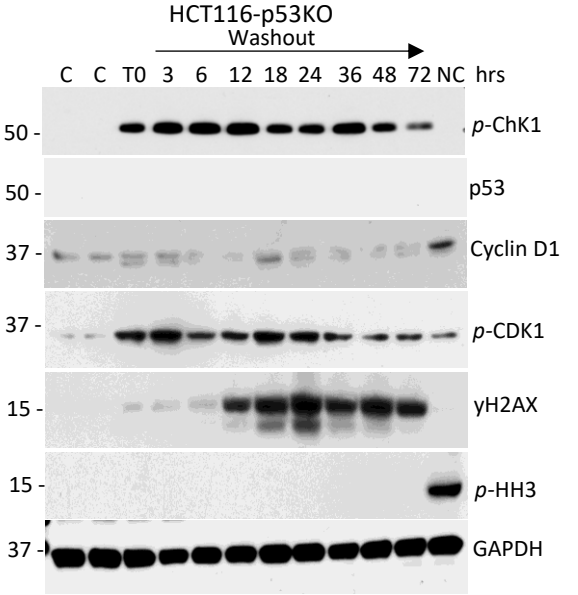
e
HCT116-p53KO
Washout
C C T0 3 6 12 18 24 36 48 72 NC hrs
p-ChK1
p53
Cyclin D1
p-CDK1
γH2AX
p-HH3
GAPDH

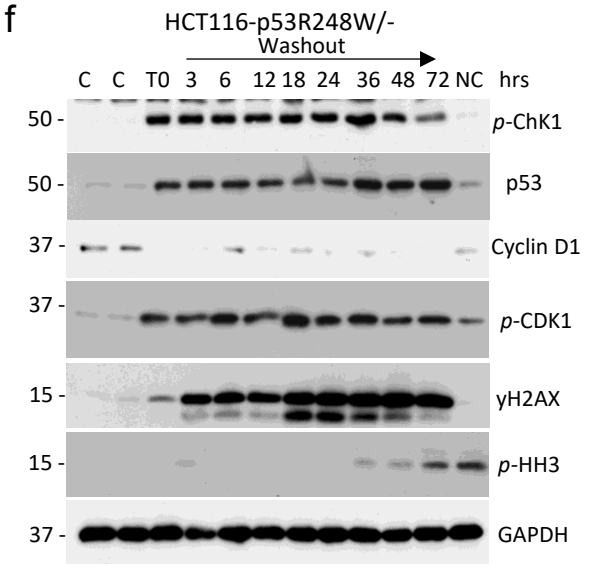
f
HCT116-p53R248W/-
Washout
C C T0 3 6 12 18 24 36 48 72 NC hrs
p-ChK1
p53
Cyclin D1
p-CDK1
γH2AX
p-HH3
GAPDH

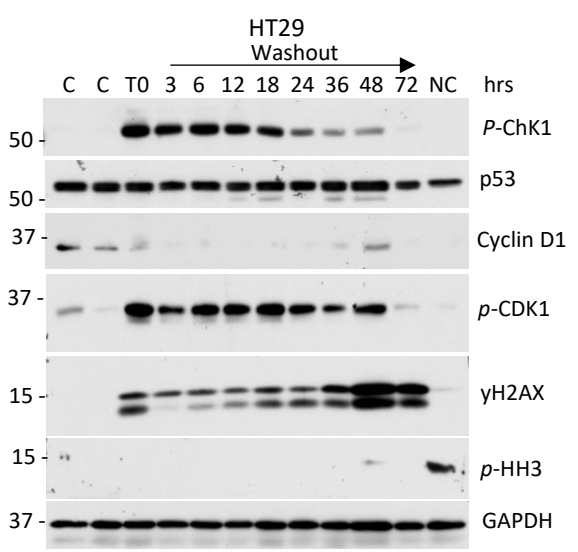
g
HT29
Washout
C C T0 3 6 12 18 24 36 48 72 NC hrs
P-ChK1
p53
Cyclin D1
p-CDK1
γH2AX
p-HH3
GAPDH

Fig. 5

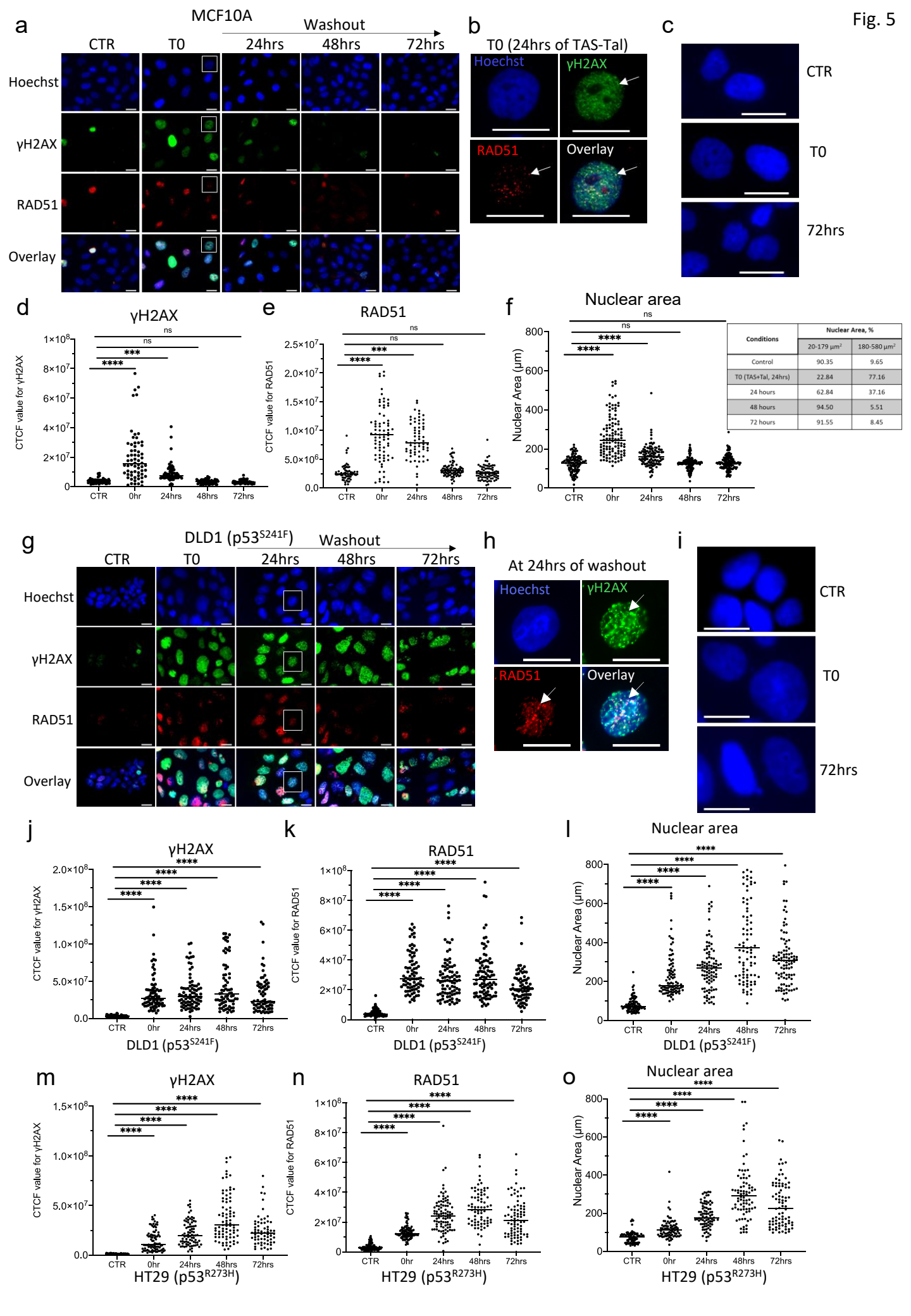

Conditions	Nuclear Area, %	
	20-179 μm²	180-580 μm²
Control	90.35	9.65
T0 (TAS+Tal, 24hrs)	22.84	77.16
24 hours	62.84	37.16
48 hours	94.50	5.51
72 hours	91.55	8.45

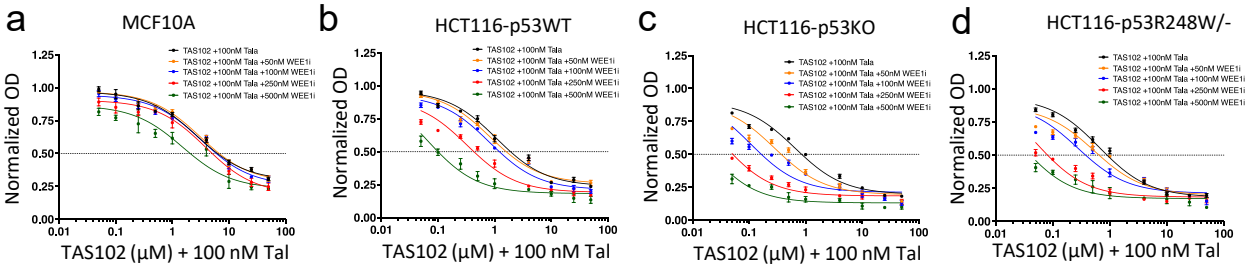

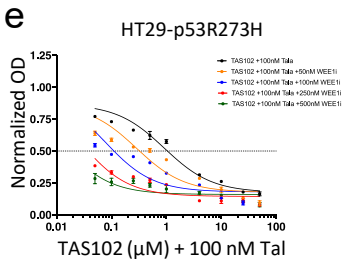

f

Cell line	p53 Status	IC50-TAS102, μM + 100nM Tal	IC50-TAS102, μM + 100nM Tal + 100nM WEE1i	Fold change at 100nM WEE1i	CI index
MCF10A	WT	3.20 ± 0.65	3.02 ± 0.36	1.07	0.94
HCT116	WT	1.19 ± 0.15	0.86 ± 0.07	1.38	0.67
HCT116	KO	0.75 ± 0.16	0.21 ± 0.15	3.57	0.31
HCT116	R248W/-	0.79 ± 0.19	0.32 ± 0.06	2.47	0.42
HT29	R273H	0.81 ± 0.16	0.12 ± 0.06	6.75	0.26

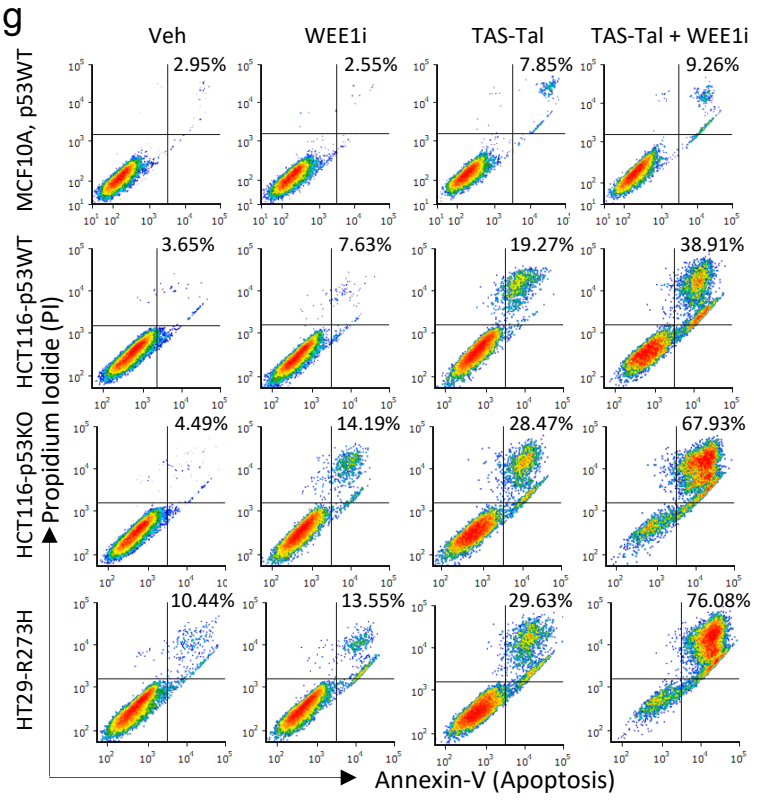

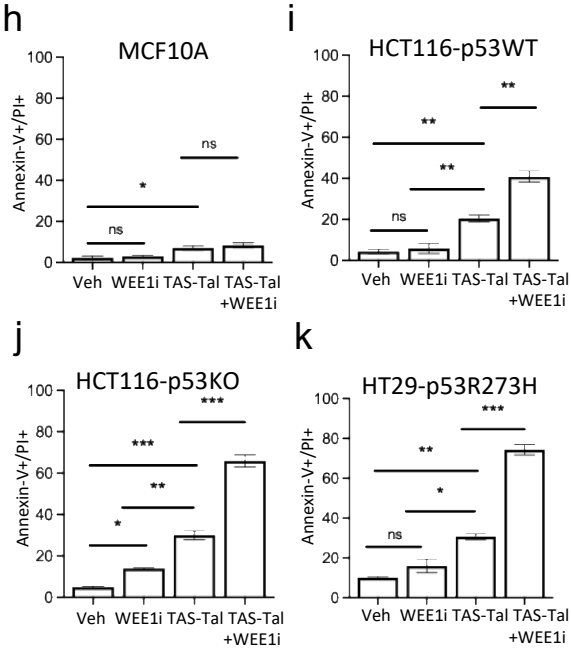

Fig. 7

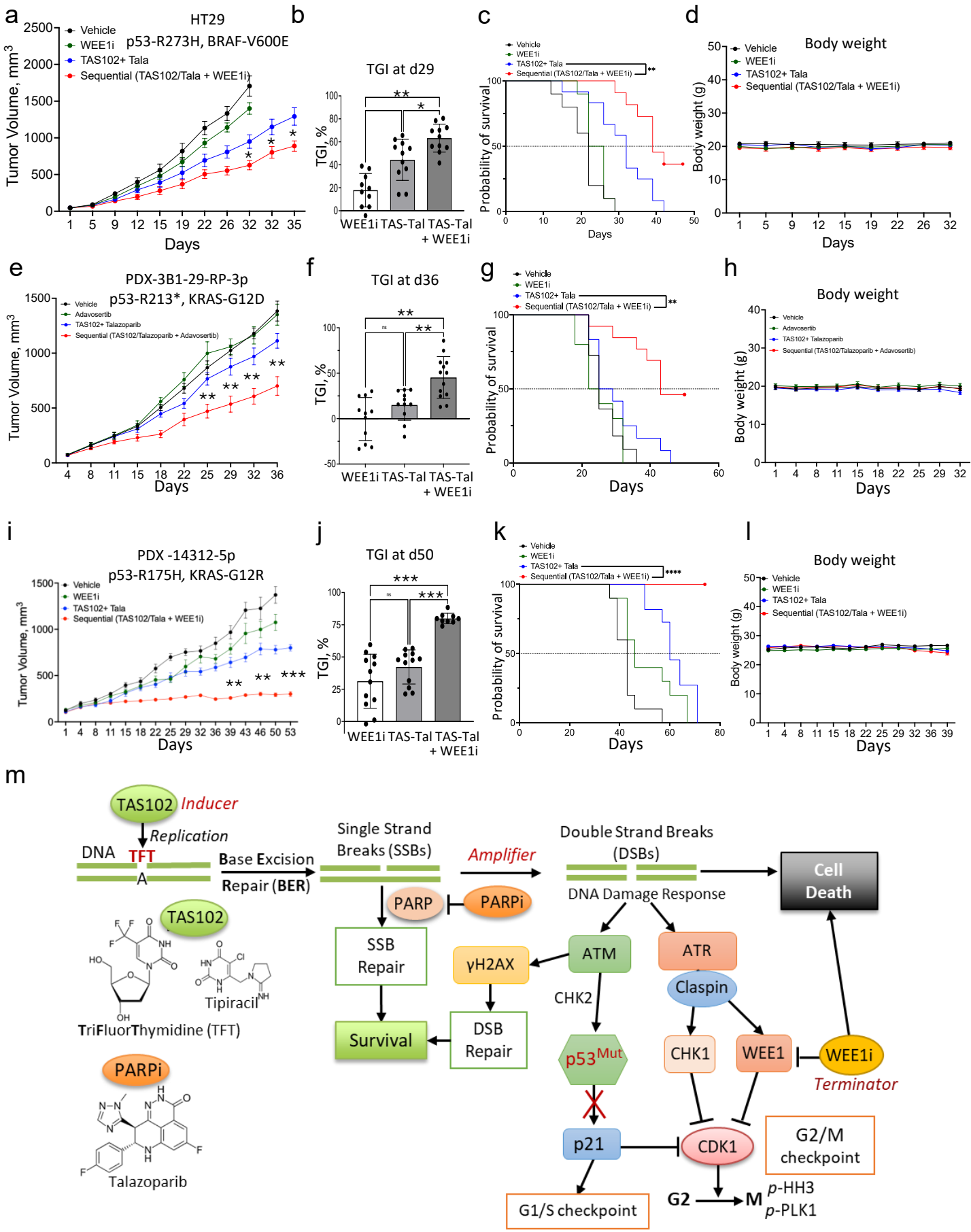
a
HT29
p53-R273H, BRAF-V600E
Vehicle
WEE1i
TAS102+ Tala
Sequential (TAS102/Tala + WEE1i)
Tumor Volume, mm3
Days
b
TGI at d29
TGI, %
WEE1i
TAS-Tal
TAS-Tal + WEE1i
c
Probability of survival
Days
d
Body weight
Body weight (g)
e
PDX-3B1-29-RP-3p
p53-R213*, KRAS-G12D
Adavosertib
TAS102+ Talazoparib
Sequential (TAS102/Talazoparib + Adavosertib)
f
TGI at d36
g
h
i
PDX -14312-5p
p53-R175H, KRAS-G12R
j
TGI at d50
k
l
m
TAS102
Inducer
Replication
DNA
TFT
A
Base Excision Repair (BER)
Single Strand Breaks (SSBs)
Amplifier
Double Strand Breaks (DSBs)
DNA Damage Response
Cell Death
PARP
PARPi
SSB Repair
γH2AX
ATM
ATR
Claspin
CHK2
Survival
DSB Repair
p53Mut
CHK1
WEE1
WEE1i
Terminator
TriFluorThymidine (TFT)
Tipiracil
Talazoparib
p21
CDK1
G2/M checkpoint
G1/S checkpoint
G2
M
p-HH3
p-PLK1